

Chemistry and Radiative Shielding in Star Forming Galactic Disks

Chalence Safranek-Shrader^{1,4*}, Mark R. Krumholz^{1,2}, Chang-Goo Kim³,
 Eve C. Ostriker³, Richard I. Klein^{4,5}, Shule Li⁴, Christopher F. McKee^{4,6}, James M. Stone³

¹*Department of Astronomy and Astrophysics, University of California, Santa Cruz, CA 95064, USA*

²*Research School of Astronomy and Astrophysics, Australian National University, Canberra, ACT 2611, Australia*

³*Department of Astrophysical Sciences, Princeton University, Princeton, NJ 08544, USA*

⁴*Astronomy Department, University of California, Berkeley, CA 94720, USA*

⁵*Lawrence Livermore National Laboratory, P.O. Box 808, L-23, Livermore, CA 94550, USA*

⁶*Physics Department, University of California, Berkeley, CA 94720, USA*

5 November 2018

ABSTRACT

To understand the conditions under which dense, molecular gas is able to form within a galaxy, we post-process a series of three-dimensional galactic-disk-scale simulations with ray-tracing based radiative transfer and chemical network integration to compute the equilibrium chemical and thermal state of the gas. In performing these simulations we vary a number of parameters, such as the ISRF strength, vertical scale height of stellar sources, cosmic ray flux, to gauge the sensitivity of our results to these variations. Self-shielding permits significant molecular hydrogen (H_2) abundances in dense filaments around the disk midplane, accounting for approximately $\sim 10 - 15\%$ of the total gas mass. Significant CO fractions only form in the densest, $n_{\text{H}} \gtrsim 10^3 \text{ cm}^{-3}$, gas where a combination of dust, H_2 , and self-shielding attenuate the FUV background. We additionally compare these ray-tracing based solutions to photochemistry with complementary models where photo-shielding is accounted for with locally computed prescriptions. With some exceptions, these local models for the radiative shielding length perform reasonably well at reproducing the distribution and amount of molecular gas as compared with a detailed, global ray tracing calculation. Specifically, an approach based on the Jeans Length with a $T = 40 \text{ K}$ temperature cap performs the best in regards to a number of different quantitative measures based on the H_2 and CO abundances.

Key words: stars: formation — stars: mass function

1 INTRODUCTION

The interstellar medium (ISM) of a typical disk galaxy is divided into variety of distinct phases, generally classified into hot ionized ($T \gtrsim 10^5 \text{ K}$) gas, the warm neutral medium (WNM; $T \sim 10^4 \text{ K}$), and the cold neutral medium (CNM; $T \lesssim 100 \text{ K}$). Star formation, however, appears to be restricted to cold dense gas with a star formation rate (SFR) that strongly correlates with the molecular gas content (Wong & Blitz 2002; Kennicutt et al. 2007; Bigiel et al. 2008; Leroy et al. 2008; Saintonge et al. 2011a,b; Leroy et al. 2013). This link between star formation and molecular gas is probably not causal, in the sense that the presence of molecules simply marks those parts of the ISM that are cold and dense enough to undergo gravitational collapse (Krumholz et al. 2011; Krumholz 2012; Glover & Clark 2012a,b), but the molecular gas nonetheless represents an indispensable tracer of star forming regions in the local and distant Universe. Understanding these crucial links between star formation, the ISM, and galaxy evolution, all intricately cou-

pled through a variety of energetic stellar feedback mechanisms, must rely on identifying the pathways and conditions under which cold, molecular gas is able to develop. Furthermore, the gas temperature sets the characteristic size ($R \propto T$) and mass ($M \propto T^2$) of prestellar cores that develop in post-shock regions within magnetized, star-forming clouds (e.g., Chen & Ostriker 2014, 2015). Since gas cooled by rotational transitions of CO is able to reach lower temperature than that cooled by fine-structure lines of atomic carbon, tracking molecular chemistry is crucial to accurately represent small-scale fragmentation in numerical simulations of star-forming clouds.

Young, massive stars are the main source of far-ultraviolet (FUV) photons that permeate the ISM and readily photodissociate interstellar molecules, such as molecular hydrogen (H_2) and carbon monoxide (CO). Molecular gas is thus found predominantly in dense, cold regions where dust shielding and self-shielding by the molecules themselves have attenuated the interstellar radiation field (ISRF) intensity far below its mean. The transition zones separating atomic and molecular gas, so called photodissociation regions (PDRs), have been studied extensively both numerically and theo-

* E-mail: ctss@berkeley.edu

retically (e.g., Federman et al. 1979; van Dishoeck & Black 1986; Sternberg 1988; Draine & Bertoldi 1996; Hollenbach & Tielens 1999; Krumholz et al. 2008; Wolfire et al. 2010; Sternberg et al. 2014; Bialy & Sternberg 2015). Typically, the outer, unshielded layers of a PDR are composed of atomic hydrogen and singly ionized carbon. As column density increases the atomic-to-molecular transition begins to occur, with the C-CO transition occurring interior to the H I-H₂ one. Deeper still, when external FUV photons have been entirely absorbed, the chemistry and thermodynamics becomes dominated by the presence of deep penetrating cosmic rays and the freeze out of molecules onto dust grains.

Simply understanding the structure of a non-dynamic, one-dimensional PDR is of limited utility. The ISM is a dynamic environment where a variety of non-linear, coupled processes determine the global distribution and state of gas. Star forming complexes are continually assembled through self-gravity, while stellar feedback acts to disperse the structures. Turbulent motions, ubiquitous in the ISM, dissipate through radiative shocks, but are continually replenished through a combination of supernovae and stellar winds. Thermal processes, such as dust grain photoelectric heating and molecular line cooling, further influence the state of the ISM and are sensitive functions of ambient radiation fields, column density, and the non-equilibrium chemical state of the gas.

Implementing these processes in a numerical simulation is highly non-trivial, a challenge further exacerbated by the enormous range of spatial scales involved; the star forming region of a galactic disk can extend radially for tens of kiloparsecs while individual star forming disks are typically hundreds of AUs and smaller, making this a computational *tour de force* for even adaptively refined grids. Nevertheless, three-dimensional simulations of finite, but representative, portions of galactic disks have attempted to replicate a supernova-driven ISM, finding success in reproducing a multiphase ISM (Joung & Mac Low 2006; Hill et al. 2012; Gent et al. 2013), or demonstrating the regulation of the SFR by stellar feedback (Hopkins et al. 2011; Shetty & Ostriker 2012; Creasey et al. 2013; Kim et al. 2011, 2013; Hennebelle & Iffrig 2014).

Studies that have examined the atomic-to-molecular transition within large-scale, three-dimensional simulations has received far less attention. Glover & Mac Low (2007a,b) and Mac Low & Glover (2012) simulated the conversion of the atomic ISM to molecular form in isolated periodic boxes, without explicit feedback but including driven or decaying turbulence. Smith et al. (2014) and Dobbs et al. (2008) included non-equilibrium H₂ formation in simulations of galactic discs, but neglected self-gravity and supernova feedback. These studies did include an H₂-dissociating FUV photo-background, though assumed it to be constant in both space and time. Walch et al. (2014) recently conducted a series of galactic scale simulations including supernova feedback, non-equilibrium chemistry, and radiative shielding based on the TreeCol algorithm (Clark et al. 2012). Here, the strength of the FUV photodissociating background scales linearly with the instantaneous SFR, though is spatially uniform. Walch et al. (2014) finds the amount and distribution of molecular gas depends sensitively on a number of parameters, in particular the precise rhythm and spatial distribution of supernovae.

While these simulations have provided insight into the relationship between dynamics and chemistry, the price of simulating 3D time-dependent chemistry is that their treatment of photodissociation, the crucial process for regulating the chemical state of the ISM, is extremely primitive. The true photodissociation and photo-heating rate at any point depends on the flux of FUV radiation integrated over all solid angles and from sources at all distances. In con-

trast, most of the chemodynamical simulations conducted to date have relied on *ad hoc* prescriptions for the dust- and self-shielding-attenuated photodissociation rates in which a single, uniform, permeating radiation field is assumed to exist in all unshielded regions, and the degree of attenuation at a point is characterized by a single characteristic column density. These prescriptions are for the most part untested, and are of unknown accuracy.

Here our goal is to perform a detailed study on the chemical state of gas in a self-consistently simulated ISM, placing special emphasis on accurately computing the molecular content with an rigorous treatment of the generation and attenuation of photodissociating FUV radiation. We do this by post-processing the supernovae driven galactic disk simulations of Kim & Ostriker (2015b) with multifrequency ray tracing and a physically motivated spatial distribution of stellar sources. This approach has the price that it discards time-dependent dynamical effects. However, it does not rely on untested approximations for the radiative transfer problem. It therefore provides a useful complement to the more approximate dynamical simulations that have appeared in the literature thus far. In particular, our approach enables tests to evaluate the accuracy of simplified shielding schemes that have been previously used.

In this paper, our main goal is to compare a number of commonly used local approximations for the degree of radiative shielding to full solutions of the radiative transfer equation, in order to gauge the effect that different approaches to radiative shielding have on the molecular abundances and temperature. For our tests, we use a density structure obtained from large-scale ISM simulations with turbulence self-consistently driven by star formation feedback, which naturally includes vertical stratification and strong density contrasts between warm and cold gas phases. We are also able to test how the distribution of molecular complexes is sensitive to parameters such as the stellar distribution and overall FUV intensity, and the relative importance of dust- and self-shielding. Our comparison of different shielding prescriptions will advise us as to the validity and best use of local shielding approximations in upcoming multidimensional simulations of star formation that we shall perform.

We organize this paper as follows. In Section 2 we describe our methodology, including a description of the simulation we apply our post-processing to, the details of our chemical network, and the numerical approach to solving the equation of radiative transfer. In Section 3 we display our results. Finally, we discuss our results and conclude in Section 4.

2 METHODOLOGY

In this paper we apply radiative and chemical post-processing to the large-scale galactic disk simulations of Kim et al. (2013) to compute the equilibrium chemical and thermal state of the disk given a realistic distribution of stellar sources, a self-consistently derived morphological structure, and multi-frequency, long-characteristics radiative transfer.

Our methodology broadly consists of two parts. First, we perform frequency dependent radiative transfer through the simulation volume, which we describe in detail in Section 2.4, supplying us with the shielding attenuated chemical photorates. Next, these photorates are passed to a chemical network, described in Section 2.2, which is then run to equilibrium, on a cell-by-cell basis, to produce a three-dimensional datacube of chemical abundances and, in a subset of our models, gas temperature (Section 2.3). In this procedure, the ray trace and chemical network integration are intricately

linked via the photodissociation rates. The chemical abundances have an effect on the global photodissociation rates, which in turn determine the chemical abundances. Given the non-local coupling between these two steps, chemical network integration and ray tracing must be carried out iteratively until convergence is obtained in the chemical abundances.

2.1 Self-consistent galactic disk simulations

The simulations of Kim & Ostriker (2015b) (hereafter K15) were run with the ATHENA code (Stone et al. 2008) which solves the equations of ideal magnetohydrodynamics on a uniform grid. The models also include self- and external-gravity, heating and cooling, thermal conductivity, Coriolis forces, and tidal gravity in the shearing box approximation to model the effect of differential galactic rotation. While K15 ran a suite of simulations with a range of magnetic field strengths and configurations, here we focus exclusively on their MB10 (solar neighborhood analog) model that has the following initial properties: gas surface density of $\Sigma_{\text{gas}} = 10 M_{\odot} \text{pc}^{-2}$, midplane density of stars plus dark matter $\rho_{\text{sd}} = 0.05 M_{\odot} \text{pc}^{-3}$, galactic rotation angular speed $\Omega = 28 \text{ km s}^{-1} \text{ kpc}^{-1}$, uniform azimuthal magnetic field of $|B_y| = 1 \mu\text{G}$, and box size $L_x = L_y = 512 \text{ pc}$, $L_z = 1024 \text{ pc}$, where the z direction is perpendicular to the disk. The computational box had a uniform resolution of $dx = 2 \text{ pc}$ in each direction such that the number of grid cells along each direction were $N_x = N_y = 256$ and $N_z = 512$.

Gas cooling, dominated by Ly α emission at high temperatures and C II fine structure emission at lower temperatures, is included by use of the fitting formula of Koyama & Inutsuka (2000),

$$\Lambda(T) = 2 \times 10^{-19} \exp\left(\frac{-1.184 \times 10^5}{T + 1000}\right) + 2.8 \times 10^{-28} \sqrt{T} \exp\left(\frac{-92}{T}\right) \text{ erg cm}^3 \text{ s}^{-1}, \quad (1)$$

where T is the gas temperature in Kelvin. Treating radiation from young, massive stars to be the main source of heating via the dust grain photoelectric effect, the gas heating rate is set to be proportional to the recent, global SFR surface density Σ_{SFR} ,

$$\Gamma = \Gamma_0 \left[\left(\frac{\Sigma_{\text{SFR}}}{\Sigma_{\text{SFR},0}} \right) + \left(\frac{J_{\text{FUV,meta}}}{J_{\text{FUV},0}} \right) \right] \text{ erg s}^{-1}, \quad (2)$$

where $\Gamma_0 = 2 \times 10^{-26} \text{ erg s}^{-1}$ is the solar neighborhood heating rate and $\Sigma_{\text{SFR},0} = 2.5 \times 10^{-3} M_{\odot} \text{ kpc}^{-2} \text{ yr}^{-1}$ is the SFR surface density in the solar neighborhood. The term $J_{\text{FUV,meta}}/J_{\text{FUV},0} = 0.0024$ accounts for a metagalactic FUV radiation field. Radiative shielding of FUV photons, an important effect at high gas column densities, is not included.

Supernova feedback is included in the form of instantaneous momentum injection at a rate proportional to the local star formation rate, as set by the free-fall time of gas with an efficiency of 1% above a critical density threshold. The momentum from each supernova is set to $p_* = 3 \times 10^5 M_{\odot} \text{ km s}^{-1}$ representing the value at the radiative stage of a single supernova remnant (see Kim & Ostriker 2015a and references therein). This approach does not form or follow the hot ($T \gg 10^5 \text{ K}$) ISM phase, but instead focuses on the self-consistent turbulent driving, dissipation, and gravitational collapse of the atomic medium, the main gas reservoir of the ISM. The absence of a hot phase will have only a minimal effect on our results, since we are mainly concerned with molecule formation processes that are restricted to much lower temperatures.

2.2 Non-equilibrium chemical network

We utilize the chemical network described in Glover et al. (2010) which we briefly summarize here. The full chemical network consists of 32 atomic and molecular species and 218 chemical and photoreactions. The abundances of only 14 of these species (H^+ , H_2 , He^+ , C^+ , O^+ , OH , H_2O , CO , C_2 , O_2 , HCO^+ , CH , CH_2 , and CH_3^+) are computed by formal integration, i.e., via solving a stiff set of coupled ordinary differential equations. The abundances of the remaining species are computed by either assuming instantaneous chemical equilibrium (as in the case of H^- , H_2^+ , H_3^+ , CH^+ , CH_2^+ , OH^+ , H_2O^+ , and H_3O^+ , species that react so rapidly as to always be close to their equilibrium abundance values) or by utilizing conservation laws (for e^- , H , He , C , and O), thus reducing the number of coupled differential equations, and computational cost, that must be integrated to solve the full chemical network.

To model photodissociation and photoionization, we take the shape and strength of the interstellar radiation field (ISRF) to follow the standard Draine (1978) field. In Habing units, the strength of the Draine field is $G_0 = 1.7$, where the Habing (1968) radiation field is defined to be

$$G_0 = \frac{4\pi \int_{\text{FUV}} J_{\nu} d\nu}{1.6 \times 10^{-3} \text{ erg cm}^{-2} \text{ s}^{-1}}, \quad (3)$$

where J_{ν} is the angle averaged specific intensity and the integral runs over the FUV range, from 6 – 13.6 eV. The photodissociation and photoionization rate for any given chemical species can be written as

$$k_{\text{thick}} = k_{\text{thin}} G_0 f_{\text{shield}} \equiv k_{\text{thin}} G_{0,\text{eff}}, \quad (4)$$

where k_{thin} is the photorate in optically thin gas (see table B2 in Glover et al. 2010), and f_{shield} is the degree by which the photorate is reduced as compared with the optically thin rate. We defer a discussion of how the shielding factors f_{shield} and unattenuated radiative intensity G_0 are determined to Section 2.4.

2.3 Thermal processes

In a subset of our models we evolve the temperature to equilibrium along with the chemical abundances. In this section we describe these heating and cooling processes.

In the low temperature, moderate density, molecular ISM, line emission originating from the rotational transitions of CO is a major source of radiative cooling. The volumetric cooling rate from CO can be written as $\Lambda_{\text{CO}} = L_{\text{CO}} n_{\text{CO}} n_{\text{H}}$. In general, the CO cooling function L_{CO} is a complicated function of temperature, density, column density, and velocity dispersion, and in a multidimensional simulation it is not feasible to self-consistently solve for the level populations in every computational cell.

Hence, we employ the DESPOTIC code (Krumholz 2014) to pre-compute the CO cooling function. Utilizing the large velocity gradient approximation, we tabulate L_{CO} as a function of n_{H_2} , temperature, and, following Neufeld et al. (1995), an effective column density per velocity \tilde{N}_{CO} defined such that

$$\tilde{N}_{\text{CO}} = \frac{n_{\text{CO}}}{|\nabla \cdot \mathbf{v}|}, \quad (5)$$

where n_{CO} is the CO number density. The local velocity divergence, $\nabla \cdot \mathbf{v}$, is computed using a three-point stencil around the cell of interest. During the computation we read in the DESPOTIC-computed cooling tables and employ tri-linear interpolation to compute the CO cooling rate as needed.

In addition to CO line cooling, we also consider fine-structure

line emission from [C II], [C I], [O I]. In the case of these species, because their lines remain optically thin under all the conditions found in our calculations, it is straightforward to solve for the level populations and compute the cooling rate directly. We use the collisional rate coefficients, atomic data, and methodology presented in Glover & Jappsen (2007).

The rate of energy exchange between gas and dust is

$$\Lambda_{\text{gd}} = \alpha_{\text{gd}} T^{1/2} (T - T_{\text{dust}}) n_{\text{H}}^2, \quad (6)$$

where $\alpha_{\text{gd}} = 3.2 \times 10^{-34} \text{ erg cm}^3 \text{ K}^{-3/2}$ is the dust-gas coupling coefficient for Mliky Way dust in H_2 dominated regions (Goldsmith 2001) and T_{dust} is the dust temperature. In principle T_{dust} can be determined self-consistently by considering dust to be in thermal equilibrium between absorption and emission, but for simplicity here we assume a constant dust temperature of $T_{\text{dust}} = 10 \text{ K}$. This should be an acceptable approximation since gas-dust coupling does not typically become important until $n \gtrsim 10^4 \text{ cm}^{-3}$, a regime not probed here.

Cooling due to the collisional excitation of atomic hydrogen, or Lyman- α , is given by (Cen 1992),

$$\Lambda_{\text{Ly}\alpha} = 7.5 \times 10^{-19} (1 + T_5^{1/2})^{-1} e^{-118348/T} n_e n_{\text{H}1}, \quad (7)$$

where $T_5 = T/(10^5 \text{ K})$, and n_e and $n_{\text{H}1}$ are the electron and neutral hydrogen densities, respectively.

The photoelectric heating rate, including recombination cooling, is given by (Bakes & Tielens 1994),

$$\Gamma_{\text{pe}} = 10^{-24} \epsilon G_{0,\text{eff}} n_{\text{H}} - 4.65 \times 10^{-30} T^{0.94} \psi^\beta n_e n_{\text{H}}, \quad (8)$$

where $G_{0,\text{eff}} = G_0 \exp(-2.5 A_V)$ is the attenuated radiation field strength described in Section 2.4, $\psi = G_{0,\text{eff}} T^{1/2} / n_e$, $\beta = 0.735/T^{0.068}$, and

$$\epsilon = \frac{0.049}{1 + 4 \times 10^{-3} \psi^{0.73}} + \frac{0.037 (T/10^4)^{0.7}}{1 + 2 \times 10^{-4} \psi} \quad (9)$$

is the photoelectric heating efficiency.

The heating rate due to cosmic ray ionization is given by

$$\begin{aligned} \Lambda_{\text{cr}} &= \zeta n_{\text{H}} q_{\text{ion}} \\ &= \zeta n_{\text{H}} (x_{\text{H}1} q_{\text{ion,H}1} + 2 x_{\text{H}2} q_{\text{ion,H}2}), \end{aligned} \quad (10)$$

where ζ is the cosmic ray ionization rate per hydrogen nucleus which we take to be $\zeta = 10^{-17} \text{ s}^{-1}$, a relatively low value that aids in the production of CO. The energy added per cosmic ray ionization q_{ion} depends on the chemical composition of the gas. For purely atomic gas we use the recommendation from Draine (2011),

$$q_{\text{ion,H}1} = 6.5 \text{ eV} + 26.4 \text{ eV} \left(\frac{x_e}{x_e + 0.07} \right)^{1/2}, \quad (11)$$

while we use a piecewise fit given in Krumholz (2014, equation B3) of numerical data from Glassgold et al. (2012) for $q_{\text{ion,H}2}$.

Note that we do not include any sort of heating due to turbulent dissipation or ambipolar diffusion, two related effects whose combined heating rate can be comparable to the cosmic ray heating rate for the low cosmic ray ionization rate we adopt here (e.g., Li et al. 2012).

2.4 Multi-angle ray trace and radiative shielding

Modeling radiation transport in full generality within a three-dimensional simulation presents a significant numerical challenge. As noted by Glover et al. (2010), the cost of multifrequency radiation transfer scales as $O(N_\nu \times N^{5/3})$, where N_ν is the number of

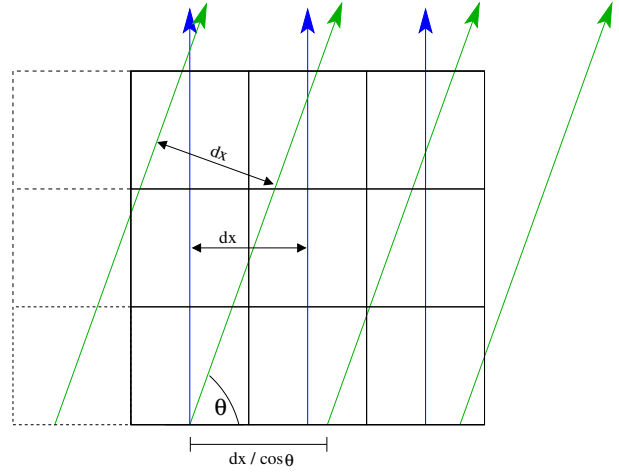


Figure 1. Two-dimensional schematic of the ray tracing procedure. Here, the first set of rays (shown as blue arrows) are launched perpendicular to the x -axis with a separation equal to the cell spacing dx . The next set of rays (green arrows) are launched with an angle of θ with respect to the x -axis and maintain a perpendicular separation dx with the first set of rays. This choice guarantees the computational domain is evenly sampled by rays for each angular set of rays. Only when the rays are physically located within the computational grid (solid boxes) is the ray tracing performed.

discrete frequency bins and N is the number of computational elements. Even with moderate resolution, this is orders-of-magnitude larger than the hydrodynamic evolution, which scales as $O(N)$, and generally intractable. While a number of approximate methods exist for solving the equation of radiative transfer in a numerical simulation

(e.g., Rijkhorst et al. 2006; Krumholz et al. 2007; Wise & Abel 2011; Davis et al. 2012), these approaches are not suitable for line transfer calculations, which are crucial for determination of the photoreaction rates. Here, we elect to solve for the radiation field, and chemical state, by direct ray-tracing applied to static simulation snapshots.

2.4.1 Shielding factors

The radiation intensity at any point along a ray is governed by the time-independent radiative transfer equation,

$$\frac{dI_\nu}{ds} = -\alpha_\nu I_\nu + j_{*,\nu}, \quad (12)$$

where I_ν is the specific intensity, α_ν is the absorption coefficient, $j_{*,\nu}$ is the emissivity, and s is the distance along the ray. We are particularly concerned with FUV photons whose dominant sources are stars with ages of $\sim 100 \text{ Myr}$ or less. Since the simulation does not follow young stars explicitly, and since by this age stars are generally no longer predominantly found in clusters (e.g., Fall & Chandar 2012; Fouesneau et al. 2014), we approximate their distribution as a smooth field that varies with height z alone. We therefore assign every grid cell a frequency-dependent FUV emissivity $j_{*,\nu} = j_{*,0,\nu} f(z)$, where the normalization $j_{*,0,\nu}$ is fixed by the requirement that the unattenuated midplane ISRF intensity, $G_{0,\text{midplane}}$, is in accordance with the current SFR surface density:

$$G_{0,\text{midplane}} = 1.7 \left(\frac{\Sigma_{\text{SFR}}}{\Sigma_{\text{SFR},0}} \right) \quad (13)$$

where Σ_{SFR} and $\Sigma_{\text{SFR},0}$ retain their definitions from Equation 2. For the vertical distribution of the FUV emissivity we adopt the profile

$$f(z) = \text{sech}^2(z/H), \quad (14)$$

appropriate for an isothermal disc, where H is the stellar scale height. For our fiducial model we adopt a scale height of $H = 100$ pc, though we do explore how variations in H affect our results.

Even in a static snapshot, solving the transfer equation in three dimensions with enough frequency resolution to resolve the dominant photodissociation lines of every important species is prohibitively expensive. Fortunately, it is also unnecessary for the purpose of computing photoreaction rates, which is our goal. Photodissociation for important interstellar species occurs via resonant absorption of an FUV photon in one or more bands that occupy a relatively narrow range of frequencies. One-dimensional simulations that include full frequency-dependent transfer show that the photodissociation rate produced by the ISRF decreases as the radiation propagates through increasing columns of material due to two main effects: continuum absorption by dust, and resonant absorption of photons near the centers of the dissociating absorption lines (van Dishoeck & Black 1986; Black & van Dishoeck 1987; van Dishoeck & Black 1988; Draine & Bertoldi 1996; Browning et al. 2003).

For dust, the reduction in the photodissociation rate is given by

$$f_{\text{shield}} = f_{\text{dust}} = \exp(-\gamma A_V) \quad (15)$$

where $\gamma = 0.92 \kappa_\nu / \kappa_V$ is the scaling between the dust opacity at the photodissociation absorption frequency and the V-band. Here κ_ν is the dust opacity evaluated at the absorption band relevant for that species, which is taken to be at a single characteristic frequency, a good approximation since κ_ν varies slowly with ν over the band; κ_V is the V-band dust opacity. For the chemical species we consider, γ ranges from 0.5 to 3.9. The visual extinction in magnitudes A_V is directly proportional to the total column density of H nuclei, $N_{\text{H}} = N_{\text{H}1} + 2N_{\text{H}2}$,

$$A_V = \frac{N_{\text{H}}}{1.87 \times 10^{21} \text{ cm}^{-2}} = N_{\text{H}} \sigma_{\text{d},V}, \quad (16)$$

where $\sigma_{\text{d},V} = 5.3 \times 10^{-22} \text{ cm}^2$ (Draine & Bertoldi 1996) is the total dust cross section in the V-band per hydrogen nucleus.

To properly model the photodissociation of H_2 and CO we must also consider self-shielding in which the molecules themselves, in addition to dust grains, contribute to the attenuation of FUV photons. Self-shielding of H_2 can be well approximated with the following analytic expression from Draine & Bertoldi (1996),

$$f_{\text{self},\text{H}_2} = \frac{0.965}{(1+x/b_5)^2} + \frac{0.035}{\sqrt{1+x}} \times \exp(-8.5 \times 10^{-4} \sqrt{1+x}), \quad (17)$$

where $x = N_{\text{H}_2} / (5 \times 10^{14} \text{ cm}^{-2})$, $b_5 = b / (10^5 \text{ cm s}^{-1})$, and $b = 9.1 \text{ km s}^{-1} (T/10^4 \text{ K})^{1/2}$ is the Doppler broadening parameter for H_2 . The total shielding factor for H_2 will be $f_{\text{shield}} = f_{\text{self},\text{H}_2} f_{\text{dust},\text{H}_2} = f_{\text{self},\text{H}_2} \exp(-3.7 A_V)$.

CO not only experiences self-shielding and dust shielding, but is additionally shielded by molecular hydrogen. The photodissociation rate for CO can be written as $k_{\text{thick}} = k_{\text{thin}} f_{\text{dust}} f_{\text{self},\text{CO}} f_{\text{CO},\text{H}_2}$, where $f_{\text{self},\text{CO}} = f_{\text{self},\text{CO}}(N_{\text{CO}})$ is the CO self-shielding function and $f_{\text{CO},\text{H}_2} = f_{\text{CO},\text{H}_2}(N_{\text{H}_2})$ accounts for the cross-shielding of CO by the overlapping Lyman-Werner lines

of H_2 . Both $f_{\text{self},\text{CO}}$ and f_{CO,H_2} are taken from Lee et al. (1996), while $f_{\text{dust}} = \exp(-2.5 A_V)$.

A critical point to realize is that, because the CO and H_2 self-shielding factors result from a rearrangement of the photon frequency distribution as radiation propagates along a ray, they may be applied independently on every ray. This means that, rather than requiring many frequency bins to resolve the dissociating lines of H_2 and CO, we can approximate the effect by considering a single frequency bin for H_2 -dissociating photons, and similarly for CO-dissociating ones, and use the pre-tabulated shielding functions to model the reduction in photodissociation rate along a ray. The main limitation in this approach is that the shielding functions have been tabulated for gas with a fixed velocity dispersion and zero bulk velocity, whereas in our simulations the velocity fields are significantly more complex. However, we show below that our results are quite insensitive to exactly how we estimate the velocity-dispersion that enters the shielding factors.

2.4.2 Solving the radiative transfer equation

Based on the discussion in the preceding section, we now discretize the equation of radiative transfer (Equation 12) by defining three distinct frequency bins: one describing radiation in the FUV dust continuum, I_{cont} , one that corresponds to the Lyman-Werner bands for H_2 , I_{H_2} , and one describing the photodissociation of CO, I_{CO} . The three frequency bins can be formally defined through the following filters:

$$\theta_{\text{FUV}}(\nu) = \theta_{\text{H}_2}(\nu) + \theta_{\text{CO}}(\nu) + \theta_{\text{cont}}(\nu), \quad (18)$$

defined such that $\theta_{\text{H}_2}(\nu)$ and $\theta_{\text{CO}}(\nu)$ equal unity in the frequency ranges that overlap with their photodissociation absorption lines, and are zero otherwise. Likewise, $\theta_{\text{cont}}(\nu) = 1$ in the FUV frequency range, excluding the photoabsorption lines of H_2 and CO, and is zero otherwise.

The intensity at any point s along a ray is given by the formal solution to Equation (12),

$$I_\nu(s) = \int_0^s \exp\left(-\int_{s'}^s \alpha_\nu ds''\right) j_{*,\nu}(s') ds'. \quad (19)$$

Identifying $\exp(-\int_{s'}^s \alpha_\nu ds'')$ to be the shielding factor f_{shield} (Equation 4) and integrating over the frequency filters defined in Equation (18) gives us the intensity in our three frequency bins:

$$I_{\text{H}_2}(s) = \int_0^\infty I_\nu(s) \theta_{\text{H}_2}(\nu) d\nu = \int_0^s f_{\text{dust}}(N'_{\text{H}}) f_{\text{self},\text{H}_2}(N'_{\text{H}_2}) j_{*,\text{H}_2}(s') ds' \quad (20)$$

$$I_{\text{CO}}(s) = \int_0^\infty I_\nu(s) \theta_{\text{CO}}(\nu) d\nu = \int_0^s f_{\text{dust}}(N'_{\text{H}}) f_{\text{self},\text{CO}}(N'_{\text{CO}}) f_{\text{CO},\text{H}_2}(N'_{\text{H}_2}) j_{*,\text{CO}}(s') ds' \quad (21)$$

$$I_{\text{cont}}(s) = \int_0^\infty I_\nu(s) \theta_{\text{cont}}(\nu) d\nu = \int_0^s f_{\text{dust}}(N'_{\text{H}}) j_{*,\text{cont}}(s') ds'. \quad (22)$$

In the above equations, the shielding factors are evaluated using the total column densities between points s and s' , $N'_{\{\text{H}/\text{H}_2/\text{CO}\}} \equiv \int_{s'}^s n_{\{\text{H}/\text{H}_2/\text{CO}\}} ds''$, $j_{*,\text{H}_2} = \int j_{*,\nu} \theta_{\text{H}_2} d\nu$, and similarly for $j_{*,\text{CO}}$ and $j_{*,\text{cont}}$

2.4.3 Spatial and angle discretization

We are now in a position to discretize the Equations (20), (21), and (22) in a way suitable for numerical calculation. Consider a ray passing through our Cartesian grid at some angle, and consider the n 'th cell along that ray. Let the sequence of cells through which the ray passes on its way to that cell n be numbered $i = 0, 1, \dots, n-1$, and let Δs_i be the path length of the ray through cell i ; let $n_{X,i}$ be the corresponding number density of species X (e.g., H_2), and similarly for all other quantities. In this case Equation (20) can be discretized to

$$I_{\text{H}_2}(n) = \sum_{i=0}^{n-1} \Delta s_i j_{*,\text{H}_2,i} f_{\text{shield}} \left(\sum_{j=i}^n n_{\{\text{H}/\text{H}_2\},j} \Delta s_j \right), \quad (23)$$

where the shielding factor, which includes both dust- and self-shielding, is evaluated using the total column $N_{\{\text{H}/\text{H}_2\}} = \sum_{j=i}^n n_{\{\text{H}/\text{H}_2\},j} \Delta s_j$ between the cells n and i . Similar results hold for Equations (21) and (22).

We have now written down a discretized version of the radiative transfer equation for a particular direction of propagation. The remaining step is to discretize the problem in angle. We do so by drawing rays in N_{pix} directions (parametrized by θ and ϕ) selected via the HEALPIX algorithm for equal area spherical discretization (Górski et al. 2005). All our models use HEALPIX level 2, corresponding $N_{\text{pix}} = 48$, which we have found provides sufficient resolution to properly sample the radiation field. For each direction, we draw through the computational domain a series of rays separated by one cell spacing dx in the direction perpendicular to the rays, such that each ray represents a solid angle $d\Omega = 4\pi/N_{\text{pix}}$ and area dx^2 . This choice guarantees that each cell is intersected by at least N_{pix} rays in total. We show a schematic diagram of our ray tracing procedure in Figure 1. The radiation intensity in any given cell is then able to be computed through an angle average of all intersecting rays.

We are ultimately interested in photodissociation rates which are in turn proportional to the angle-averaged intensity,

$$k_{\text{thick},\text{H}_2} \propto J_{\text{H}_2} = \frac{1}{4\pi} \int I_{\text{H}_2} d\Omega, \quad (24)$$

and similarly for all other species. Evaluating this integral requires some subtlety; although all our rays represent an equal amount of solid angle, not all rays intersecting a cell have the same path length Δs through it, even rays that represent the same direction of radiation propagation. The contribution to the mean intensity in a cell from a given ray n will be proportional to the time that the photons propagating along that ray spend in the cell, and thus proportional to Δs_n . We therefore compute the mean intensity by weighting each ray's contribution by Δs :

$$J_{\text{H}_2} \propto \left(\sum_{n=1}^{N_{\text{ray}}} I_{\text{H}_2,n} \Delta s_n \right) / \left(\sum_{n=1}^{N_{\text{ray}}} \Delta s_n \right) \quad (25)$$

where N_{ray} is the total number of rays that intersected the cell. The conversion between J_{H_2} and $k_{\text{thick},\text{H}_2}$ is implicitly performed through a proper choice of the normalization of the FUV cell emissivity, $j_{*,\nu,0}$.

2.5 Local approximations for radiative shielding

We are interested in comparing the results obtained with the full angle-dependent ray-trace in the previous section to those produced

by various local approximations for the degree of radiative shielding that have been proposed. In these approximations, the factor by which a chemical species' photodissociation rate is reduced relative to its optically thin rate, f_{shield} , is solely dependent on an effective column density: N_{H} in the case of dust shielding, and N_{H_2} or N_{CO} in the case of H_2 and CO shielding. Working under the approximation of uniform density and chemical composition, we can rewrite column density as the product of number density and some shielding length scale, $\{N_{\text{H}}, N_{\text{H}_2}, N_{\text{CO}}\} = \{n_{\text{H}}, n_{\text{H}_2}, n_{\text{CO}}\} \times L_{\text{shield}}$. This significantly reduces the complexity and computational expense of multidimensional, multifrequency radiative transfer to the relatively simple task of computing an appropriate, physically motivated shielding length L_{shield} .

Various physically motivated expressions for L_{shield} have been proposed and utilized, to varying degrees of success. The Sobolev approximation, alternatively known as the large velocity gradient (LVG) approach, was originally devised by Sobolev (1960) to study expanding stellar envelopes, but has been used extensively in simulations to model the photodissociation of H_2 (e.g., Yoshida et al. 2006; Greif et al. 2011; Stacy et al. 2013; Greif et al. 2013; Safranek-Shrader et al. 2015). It relies on the observation that in regions with a constant velocity gradient dv_r/dr , a photon will see Doppler shifted absorption lines with respect to its emission frame. Sobolev (1960) proposed that once a photon is Doppler shifted by one thermal linewidth, the photon should be free to escape. Thus, we can define the Sobolev length to be

$$L_{\text{sob}} = \frac{c_s}{|\nabla \cdot \mathbf{v}|} \quad (26)$$

where c_s is the local sound speed and the local velocity divergence $\nabla \cdot \mathbf{v}$ serves as a multidimensional analog to dv_r/dr .

The Jeans length

$$L_{\text{J}} = \left(\frac{\pi c_s^2}{G\rho} \right)^{1/2} \quad (27)$$

is the critical length scale under which the force of gravity overwhelms outward thermal pressure allowing gravitational collapse to proceed. The Jeans length is a common approximation for L_{shield} , with the physical justification that at the center of a gravitationally collapsing core, the radiative background will be attenuated by a column of gas with a length scale approximately equal to L_{J} .

We also investigate a shielding length based on the local density and its gradient such that

$$L_{\text{dens}} = \frac{\rho}{|\nabla \rho|}. \quad (28)$$

The density gradient approach has been used by Gnedin et al. (2009) to account for the self-shielding of H_2 from photodissociating radiation and provided reasonable accuracy in the column density range $3 \times 10^{20} \text{ cm}^2 < N_{\text{H}} < 3 \times 10^{23} \text{ cm}^2$.

An additional method to account for radiative shielding is to utilize the results of a full ray trace run to calibrate a relationship between density and column density (or equivalently, visual extinction). We will show in Section 3, this relationship can be approximated as

$$L_{\text{powerlaw}} \propto n_{\text{H}}^{0.42}. \quad (29)$$

which holds above a density of $\sim 10 \text{ cm}^{-3}$ and becomes increasingly accurate with increasing density. This method naturally has the disadvantage that it is perhaps unique to the particular physical system one is examining which detracts from its generality.

A highly simplified approach to account for radiative shielding is to assume that all shielding in a given cell is due to matter in the cell in question, such that $L_{\text{shield}} = dx = 2 \text{ pc}$. This

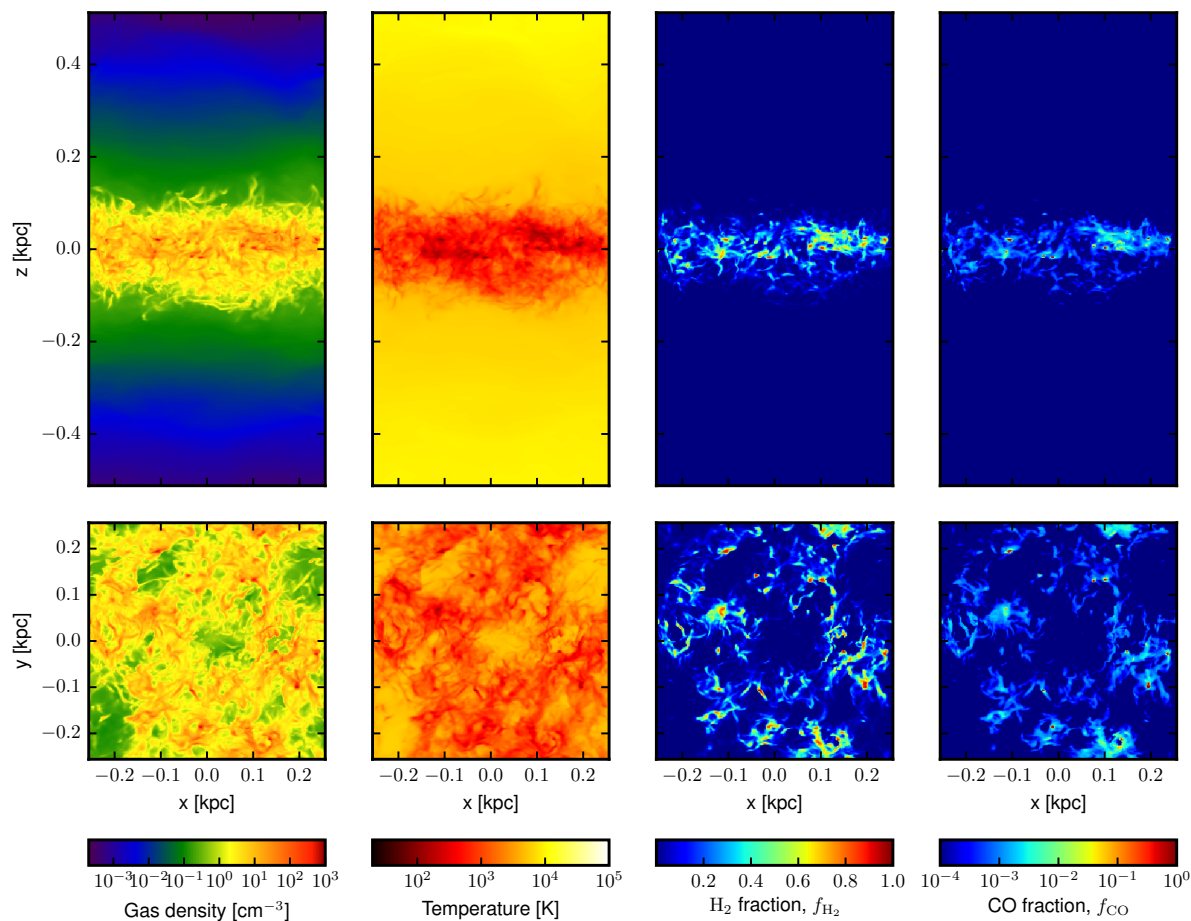


Figure 2. Mass-weighted projections of density, temperature, H_2 fraction, and CO fraction, from left-to-right, respectively. The top row are y -axis (disk edge on) projections while the bottom is z -axis (face on) projections. Note that f_{H_2} is displayed on a linear scale between 0 and 1, while f_{CO} uses a logarithmic scale.

‘single-cell’ approximation will surely underestimate the degree of radiative shielding, and thus molecular chemical abundances, as compared with the fiducial ray-tracing model, allowing limits to be placed on the effectiveness of radiative shielding.

Finally, while not a strictly local approach, we perform a model where ray tracing is only performed over the six directions aligned with the Cartesian axes, instead of the 48 HEALPIX selected directions in the ray trace models. This approach, known as the six-ray approximation, can be computationally efficient since the transport of rays exploits the alignment of the grid. It is a compromise between a local approach and full-fledged, multi-angle radiative transfer.

For this to be a clean comparison, the local and ray-trace models need to utilize the same unattenuated radiation field G_0 so that the sole difference between the various methodologies is in the computation of f_{shield} . To achieve this, in the local models we begin by performing the multiangle ray-trace procedure described in Section 2.4, but with all radiative shielding turned off, $f_{\text{shield}} = 1$, providing us with the unattenuated radiation field G_0 in each grid cell. This unattenuated field is then used in Equation 4, along with the locally determined f_{shield} , to compute the chemical photodissociation rates.

3 RESULTS

In our fiducial runs, we apply the method described in Section 2.4 to three static snapshots from the simulations of K15. Hereafter these three fiducial runs will be labeled as F1, F2, and F3. The major difference between these snapshots is the SFR (as determined in K15 by counting the number of supernovae within the last 10 Myr) which translates into differing normalizations of the midplane, and global, FUV intensities. Models F1, F2, and F3 have, respectively, midplane FUV intensities of 0.36, 0.39, and 0.65 when normalized to the Habing field¹. All the physics described in Sections 2.2 through 2.4.3 is included, with the exception that the temperature is held constant. We additionally run models where key physical parameters are varied, or a particular physical effect is switched off, to gauge the sensitivity of our results to these variations. These

¹ Note that these FUV intensities are $\sim 3 - 5$ less than the interstellar average of 1.7. This stems in part from the choice of snapshot from K15; all the snapshots selected from K15 were chosen due to the presence of large amounts of dense gas just on the verge of forming stars, and a correspondingly below average instantaneous star formation rate Σ_{SFR} . Since the FUV intensity in K15 depends linearly on Σ_{SFR} , this resulted in the chosen snapshots having a below average mean FUV intensity.

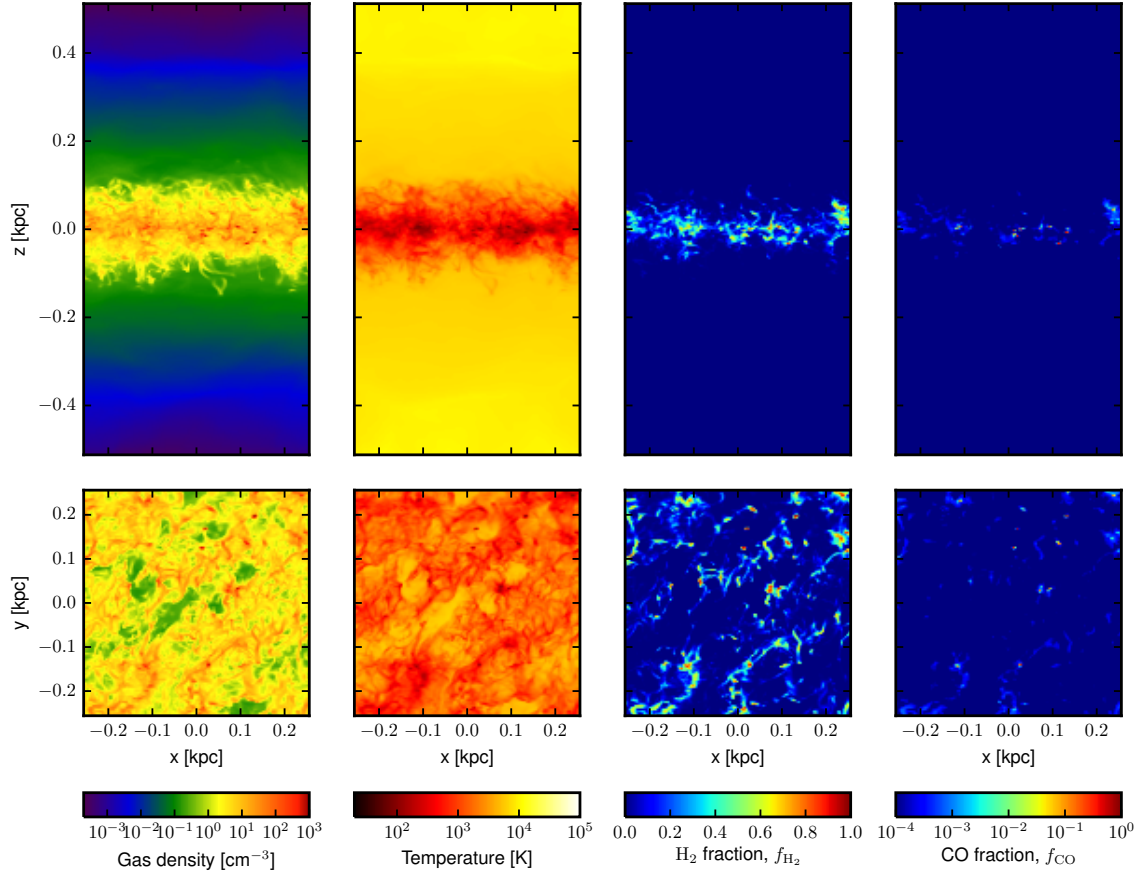


Figure 3. Same as Figure 2 but for model F2

models are otherwise identical to the fiducial model F1 and are labeled as follows:

- 1) V1: Stellar density scale height decreased to $H = 20$ pc (Equation 14), down from our fiducial value of 100 pc.
- 2) V2: Stellar density scale height increased to 200 pc.
- 3) V3: No self-shielding or cross-shielding for H_2 or CO ($f_{\text{self},\text{H}_2} = f_{\text{self},\text{CO}} = f_{\text{CO},\text{H}_2} = 1$).
- 4) V4: No H_2 self-shielding ($f_{\text{self},\text{H}_2} = 1$).
- 5) V5: No CO self- or cross-shielding ($f_{\text{self},\text{CO}} = f_{\text{CO},\text{H}_2} = 1$).
- 6) V6: No dust shielding for H_2 and CO. Dust shielding is still included for every other chemical species.
- 7) V7: Normalization of the midplane FUV intensity is increased by a factor of 10.
- 8) V8: Normalization of the midplane FUV intensity is decreased by a factor of 10.
- 9) V9: Cosmic ray ionization rate increased by a factor of 10 to $\zeta = 10^{-16} \text{ s}^{-1}$, more consistent with recent measurements (e.g., Indriolo & McCall 2012).
- 10) V10: All radiative shielding turned off.

We present two models where the temperature, in addition to the chemical abundances, is evolved:

- 1) T1: Temperature is evolved in addition to chemical abundances, otherwise identical to model F1.
- 2) T2: Temperature is evolved in addition to chemical abundances, and all radiative shielding turned off.
- 3) T3: Temperature is evolved in addition to chemical abundances, and the midplane FUV intensity is increased by a factor of 10, like in model V7.
- 4) T3: Temperature is evolved in addition to chemical abundances, and the midplane FUV intensity is decreased by a factor of 10, like in model V8.

Finally, we run models where the local approximations described in Section 3.4, instead of the ray-tracing machinery, are utilized to account for radiative shielding. We label these models as follows:

- 1) L1: $L_{\text{shield}} = L_J$ (Equation 27)
- 2) L1a: $L_{\text{shield}} = L_J$, though with a temperature ceiling of 40 K used in the evaluation of L_J .
- 3) L2: $L_{\text{shield}} = L_{\text{sobolev}}$ (Equation 26)

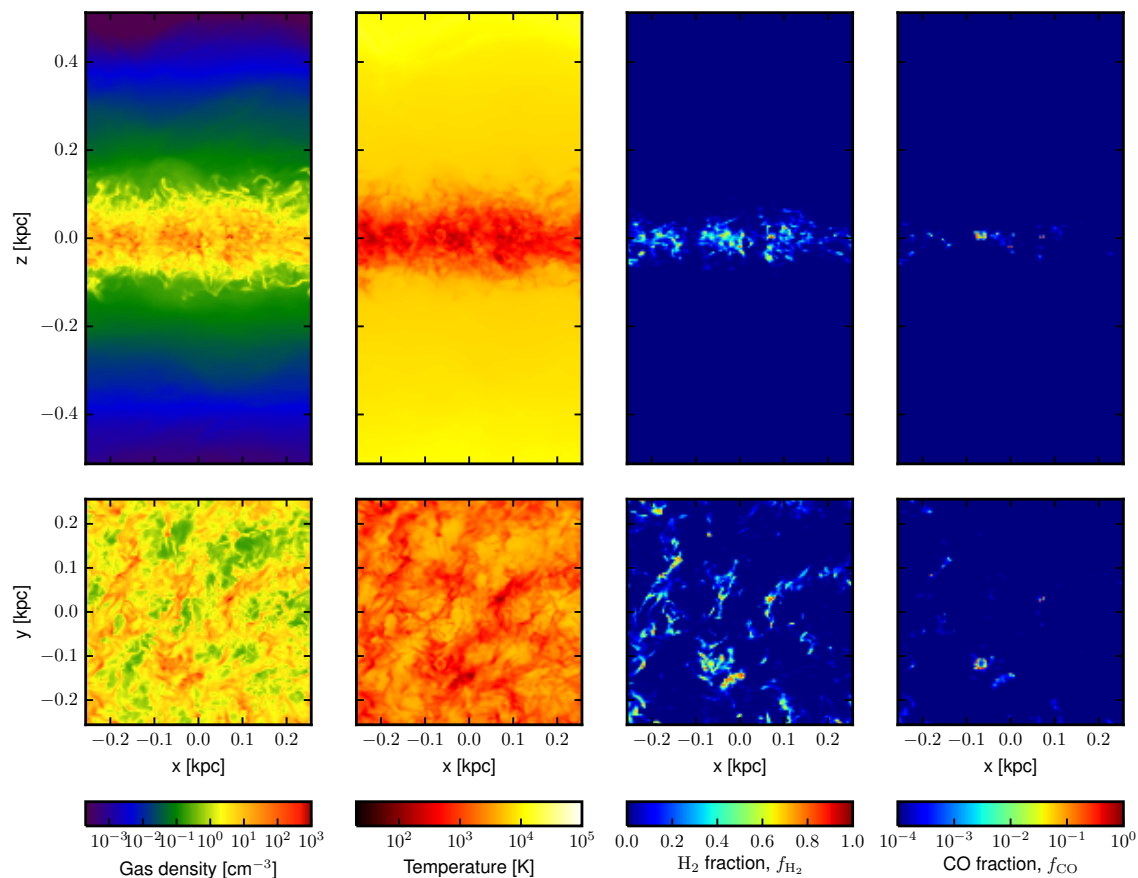


Figure 4. Same as Figure 3 but for model F3.

- 4) L3: $L_{\text{shield}} = L_{\text{dens}}$ (Equation 28)
- 5) L4: L_{shield} calibrated to be a function of density from results of fiducial models (Equation 29).
- 6) L5: $L_{\text{shield}} = dx = 2 \text{ pc}$, the local cell size; radiative shielding is only included from a single cell.
- 7) L6: Six-ray approximation. Not strictly a local quantity, though still a commonly employed approximation to the full radiative transfer problem.

In Table 1 we summarize the parameters of each model, and in Table 2 we provide various quantitative measures for each model, including the total mass fraction of H_2 , CO, and a number of comparison measures with the fiducial run F1. This table will serve as a useful global comparison between each model we consider and will be referenced often in the remainder of the text.

3.1 Fiducial models: F1-F3

In Figures 2 through 4 we show the results of models F1, F2, and F3, the fiducial runs with ray-tracing. In each of these figures the left two columns are mass-weighted projections of gas density

and temperature, representing the original data of K15 unchanged by our analysis. The right two columns of Figures 2-4 are mass-weighted projections of the H_2 and CO fractions, $f_{\text{H}_2} \equiv 1 - f_{\text{H}_1}$ and f_{CO} , the primary quantitative outputs of this study. These fractions are defined such that an H_2 fraction of unity corresponds to all hydrogen being in the form of H_2 while equivalently $f_{\text{CO}} = 1$ corresponds to all carbon atoms being incorporated in CO molecules. As is evident in all three snapshots, the bulk of the molecular gas is located close to the galactic midplane, within a vertical distance of roughly 80 pc. A prerequisite for molecules to form is the availability of dense, $n_{\text{H}} \gtrsim 10 \text{ cm}^{-3}$, gas, controlled mainly by vertical stratification of pressure and the heating rate, which together define whether thermal equilibrium admits a cold phase. In the simulations of K15, two phases are always present at the midplane (see also Ostriker, McKee, & Leroy 2010), but at high latitudes the pressure is too low for the formation of a cold phase. Morphologically, H_2 is found predominantly along dense, filamentary structures that formed as a result of supernovae-driven turbulence in the parent simulation of K15. In model F1 roughly 20% of all gas has an H_2 fraction f_{H_2} exceeding 0.5 (Table 2). This $f_{\text{H}_2} > 0.5$ mass fraction

Table 1. Name and description for each model.

Model Name	H [pc]	Radiative shielding ¹			Midplane G_0	ζ^2 [s ⁻¹ H ⁻¹]	Temp	RT Method
		H ₂	CO	Dust				
Fiducial								
F1	100	✓	✓	✓	0.36	10 ⁻¹⁷	Fixed	Ray Trace
F2	100	✓	✓	✓	0.39	10 ⁻¹⁷	Fixed	Ray Trace
F3	100	✓	✓	✓	0.65	10 ⁻¹⁷	Fixed	Ray Trace
Variation								
V1	20	✓	✓	✓	0.36	10 ⁻¹⁷	Fixed	Ray Trace
V2	200	✓	✓	✓	0.36	10 ⁻¹⁷	Fixed	Ray Trace
V3	100			✓	0.36	10 ⁻¹⁷	Fixed	Ray Trace
V4	100		✓	✓	0.36	10 ⁻¹⁷	Fixed	Ray Trace
V5	100	✓		✓	0.36	10 ⁻¹⁷	Fixed	Ray Trace
V6	100	✓	✓		0.36	10 ⁻¹⁷	Fixed	Ray Trace
V7	100	✓	✓	✓	3.6	10 ⁻¹⁷	Fixed	Ray Trace
V8	100	✓	✓	✓	0.036	10 ⁻¹⁷	Fixed	Ray Trace
V9	100	✓	✓	✓	0.36	10 ⁻¹⁶	Fixed	Ray Trace
V10	100				0.36	10 ⁻¹⁷	Fixed	Ray Trace
Temperature								
T1	100	✓	✓	✓	0.36	10 ⁻¹⁷	Evol	Ray Trace
T2	100				0.36	10 ⁻¹⁷	Evol	Ray Trace
T3	100	✓	✓	✓	3.6	10 ⁻¹⁷	Evol	Ray Trace
T4	100	✓	✓	✓	0.036	10 ⁻¹⁷	Evol	Ray Trace
Local								
L1	100	✓	✓	✓	0.36	10 ⁻¹⁷	Fixed	Jeans
L1a	100	✓	✓	✓	0.36	10 ⁻¹⁷	Fixed	Jeans w/ T ceiling
L2	100	✓	✓	✓	0.36	10 ⁻¹⁷	Fixed	Sobolev
L3	100	✓	✓	✓	0.36	10 ⁻¹⁷	Fixed	Dens grad
L4	100	✓	✓	✓	0.36	10 ⁻¹⁷	Fixed	Power-law
L5	100	✓	✓	✓	0.36	10 ⁻¹⁷	Fixed	Single-cell
L6	100	✓	✓	✓	0.36	10 ⁻¹⁷	Fixed	Six-ray

Notes — (1) Radiative shielding and its subheaders denote the inclusion of a given form of radiative shielding. H₂ stands for H₂ self-shielding, CO denotes both CO self-shielding and cross-shielding of CO by H₂, and Dust refers to the shielding of H₂ and CO by dust grains. (2) ζ refers to the cosmic ray ionization rate per second per hydrogen nucleus.

drops to 15% and 10% for models F2 and F3 which have, respectively, elevated midplane FUV intensities of $G_0 = 0.39$ and 0.65.

It is instructive to additionally consider a subset of the simulation volume, where the assumption of chemical equilibrium is well justified, for much of our analysis. Hereafter, we define *cold, dense gas* to be that with a density $n_{\text{H}} > 100 \text{ cm}^{-3}$ and temperature $T < 100 \text{ K}$; quantitative justification for these values based on the chemical equilibrium timescale is discussed in Section 4. In addition, these cold, dense gas clumps are more analogous to observed star forming clouds or clumps (e.g., Bergin & Tafalla 2007). By mass, approximately 3% (2%) of gas within models F1 and F2 (F3) can be classified as cold, dense in which 100% of gas has $f_{\text{H}_2} > 0.5$, with corresponding average mass fractions of $f_{\text{H}_2} = 0.74$ for models F1-F3. It is important to note that the H₂ fraction in low and moderate-density regions is likely an overestimate since it is computed under the assumption of chemical equilibrium, a simplification we discuss further in Section 4.

Compared to H₂, the global CO fractions are significantly smaller in models F1, F2, and F3. In models F1 and F2, the total mass fraction of gas with a CO fraction $f_{\text{CO}} > 0.5$ is $\approx .3\%$ and three times less for model F3. In cold, dense gas this fraction increases to $\approx 10\%$ for models F1 and F2 and 6% for F3. Significant fractions of CO ($f_{\text{CO}} > 0.1$) are only marginally visible in Figures 2-4 (note the differing scale between the H₂ and CO projections)

and are restricted to the densest gas ($n_{\text{H}} \gtrsim \text{few} \times 10^2 \text{ cm}^{-3}$) in small ($\sim 5 - 10 \text{ pc}$), clumpy structures. Diffuse CO (defined here as $0.1 > f_{\text{CO}} > 10^{-4}$) is slightly more widespread and tends to trace the distribution of H₂ and dense gas.

We explore the relationship between the H₂ and CO abundances, density, and effective visual extinction in Figure 5 for model F1. Here we show phase plots of molecular hydrogen and CO abundance as a function of gas density and effective visual extinction. Since the ray-trace models do not explicitly assign a distinct A_{V} to each cell (unlike models L1-L5 that utilize a local approximation), we define the effective visual extinction from dust $A_{\text{V,eff}}$ to be the value that would produce an identical $G_{0,\text{eff}}$ as compared with a ray-trace model, i.e.,

$$A_{\text{V,eff}} \equiv -\ln(f_{\text{dust}}) = -\ln\left(\frac{G_{0,\text{eff}}}{G_0}\right), \quad (30)$$

where G_0 is the unattenuated radiation field and $G_{0,\text{eff}}$ is the dust-shielding attenuated radiation field as defined in Equation (15) with $\gamma = 1$. The H1 to H₂ transition (defined when $f_{\text{H}_2} = 0.5$) occurs around a density of 20 cm^{-3} , though more sharply over a range of effective visual extinction from $\sim 0.4 - 0.7$. This agrees nicely with the analytic prediction from Sternberg et al. (2014, Equation 40) for the total atomic hydrogen column density before the H1 to

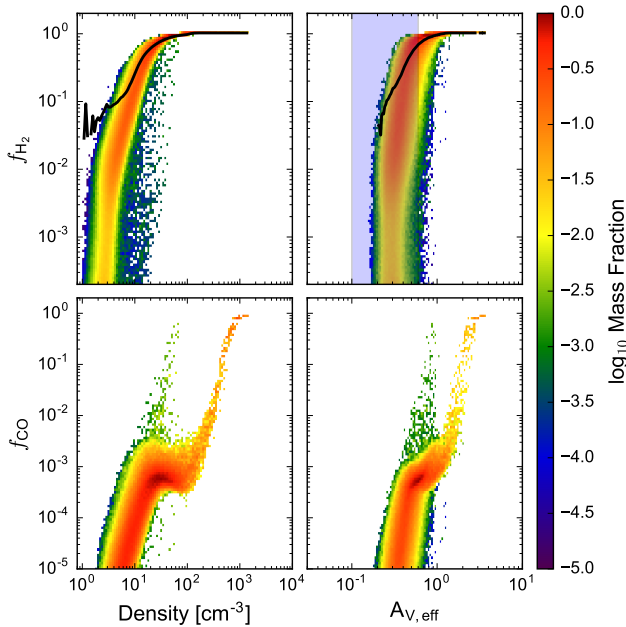


Figure 5. Phase plots of molecular hydrogen fraction versus density (top-left), molecular hydrogen fraction versus effective visual magnitude ($A_{V,\text{eff}}$, top-right), CO fraction versus density (bottom left), and CO fraction versus $A_{V,\text{eff}}$ (bottom-right). Color corresponds to the mass-fraction that particular region of phase space. For comparison, the overplotted black lines are approximate analytic expressions for the H_2 fraction (Krumholz et al. 2009; McKee & Krumholz 2010), mass-weighted in density (left panel) or $A_{V,\text{eff}}$ (right panel) bins. The shaded region in the top-right panel denotes the analytic prediction from Sternberg et al. (2014, Equation 40) for the maximum visual extinction before the H I- H_2 transition, for densities from 1 to 10 cm^{-3} .

H_2 transition, which ranges from $A_{V,\text{eff}} = 0.1$ to 0.6 for densities of 10 and 1 cm^{-3} , respectively.

Above $n_{\text{H}} = 10^2 \text{ cm}^{-3}$, gas is composed primarily of H_2 . There is less scatter and a stronger relationship between f_{H_2} and density as compared with f_{H_2} and $A_{V,\text{eff}}$, in the sense that a broad range of H_2 concentrations can exist at the same $A_{V,\text{eff}}$, particularly below $A_{V,\text{eff}} \approx 0.8$. As we will argue in Section 3.2, this lack of correlation stems from dust shielding (which depends on the total column density) being relatively unimportant in determining the H_2 abundance; instead, self-shielding is the primary mechanism that depresses the H_2 photodissociation rate and determines f_{H_2} , which of course depends on N_{H_2} , not N_{H} .

Interior to the H I to H_2 transition, the C I/C II to CO transition occurs sharply, at a density of $\approx 6 \times 10^2 \text{ cm}^{-3}$ or $A_{V,\text{eff}} \approx 2$. There also exists a second, lower density branch towards high f_{CO} , though with a thermally and observationally insignificant mass fraction. The bottom panels of Figure 5 furthermore emphasize how little carbon has fully converted into CO. This is predominantly a result of the feedback recipe used by K15, which injects momentum (representing expanding supernova blast waves) the instant density exceeds the star formation threshold, rather than allowing any time delay, a potential limitation we discuss further in Section 4.

It is interesting to examine how our methodology, which integrates a chemical network to equilibrium, compares with alternative approaches where the H_2 abundance is computed with relatively simple analytic expressions that depend solely on the unattenuated radiation field G_0 , mean absorption optical depth to

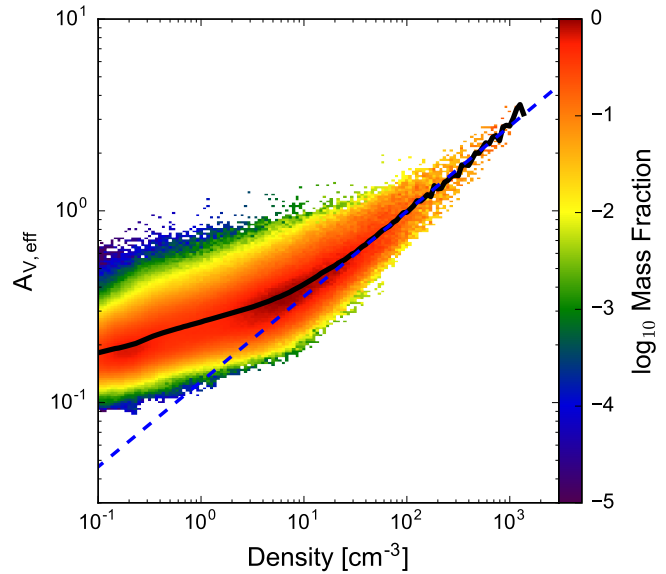


Figure 6. Relationship between density and effective visual extinction ($A_{V,\text{eff}}$, Equation 30) in model F1. The color coding represents the mass fraction within a particular region of phase space while the black line represents the mass-weighted average. The blue dashed line is a power-law fit to the average above $n_{\text{H}} = 10 \text{ cm}^{-3}$. Our best fitting parameters suggest $A_{V,\text{eff}} \propto n_{\text{H}}^{0.42}$ for $n_{\text{H}} > 10 \text{ cm}^{-3}$.

FUV photons $\tau \approx 0.5 A_V$, and density n_{H} . In a series of papers, Krumholz et al. (2008, 2009) and McKee & Krumholz (2010) analytically studied the atomic-to-molecular transition in isotropically irradiated molecular clouds. They found the H_2 fraction to be well described by the following expression:

$$f_{\text{H}_2} = 1 - \left(\frac{3}{4}\right) \frac{s}{1 + 0.25s}, \quad (31)$$

where

$$s = \frac{\ln(1 + 0.6\chi + 0.01\chi^2)}{0.6\tau}, \quad (32)$$

and

$$\chi = 42 G_0 / n_{\text{H}}. \quad (33)$$

In Figure 5 we overplot mass-weighted averages of f_{H_2} computed with Equation 31 on top of the H_2 phase plots extracted from model F1. Above $f_{\text{H}_2} \sim \text{few} \times 10^{-2}$, the expression from McKee & Krumholz (2010) does an impressive job at matching the results from our fiducial model, particularly when viewed as a function of density.

An additional result that can be extracted from our fiducial models is the relationship between gas density and effective visual extinction (Equation 30), which we plot in Figure 6 for model F1. Above a density of 10 cm^{-3} , a rough power-law relationship begins to develop between n_{H} and $A_{V,\text{eff}}$. From $n_{\text{H}} = 10 \text{ cm}^{-3}$ to 10^3 cm^{-3} , the scatter in $A_{V,\text{eff}}$ at a particular density decreases by roughly a factor of two. A least-squares fit yields the relationship $A_{V,\text{eff}} \approx (n_{\text{H}}/100 \text{ cm}^{-3})^{0.42}$, plotted in Figure 6 as a blue-dashed line. The exact normalization (100 cm^{-3} , in the previous equation) of this relationship depends on the checkpoint to which this analysis is applied, but the exponent of 0.42 appears robust between models F1, F2, and F3. This fit is the basis for one of locally de-

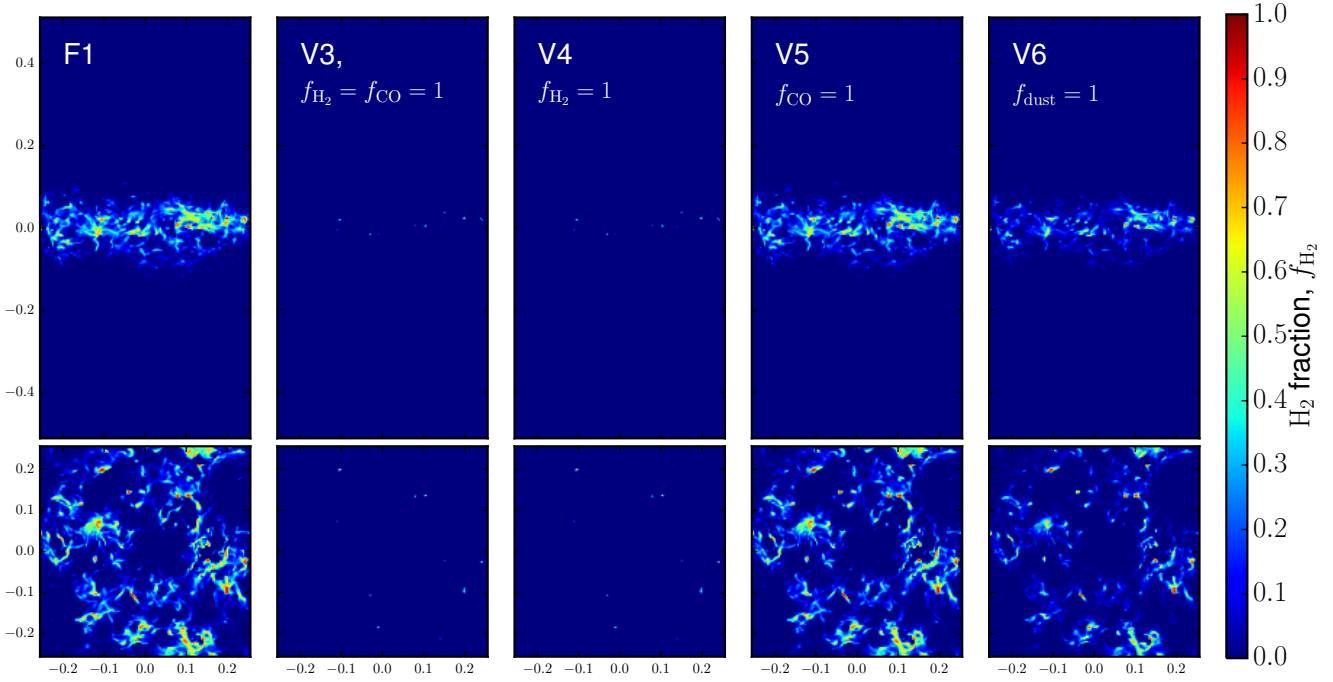


Figure 7. Mass weighted projections of H₂ exploring the role that differing types of shielding play in regulating the molecular abundances. Model V3 does not include H₂ nor CO self-shielding (only dust shielding), model V4 does not include H₂ self-shielding, and model V5 does not include CO self-shielding (here, we refer to the cross-shielding of CO by H₂ as self-shielding). Model V6 does not include dust shielding for H₂ and CO. Clearly, H₂ self-shielding is necessary for a molecule rich midplane, while dense ($n \gtrsim 10^3 \text{ cm}^{-3}$) clumps will be predominantly molecular regardless self-shielding operates or not. The removal of dust shielding results in a rather modest reduction of the H₂ fraction.

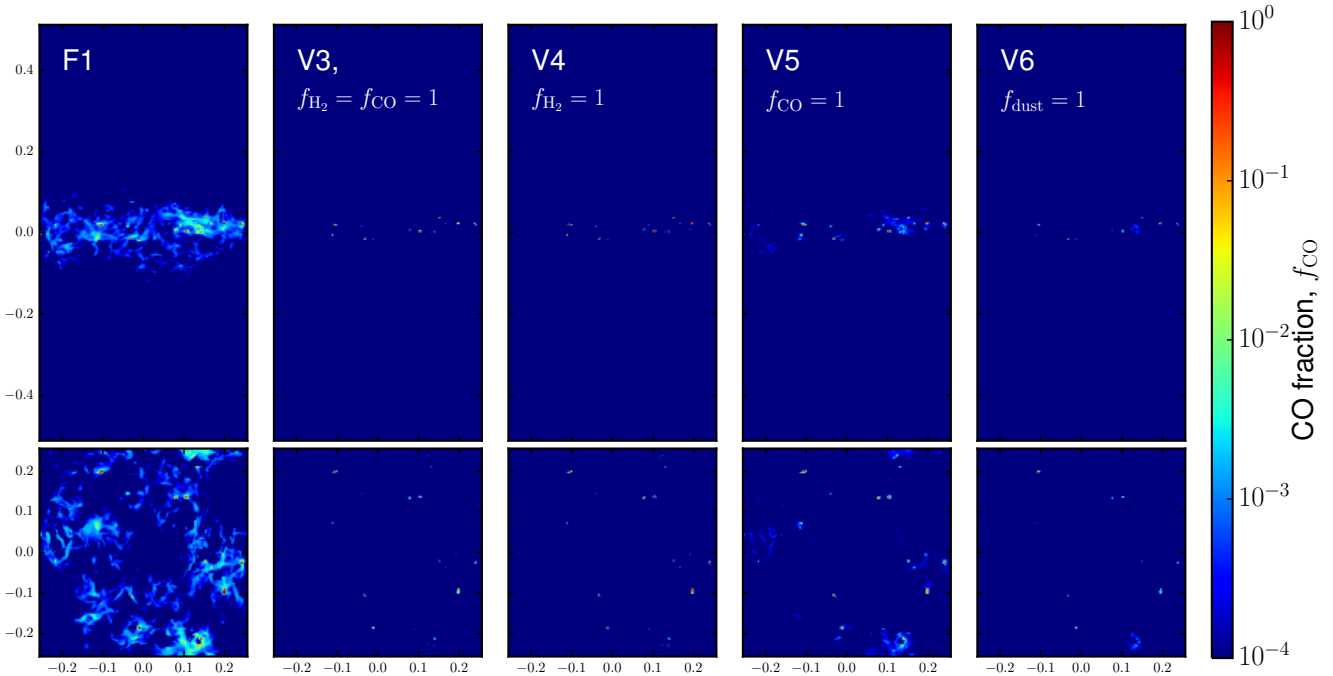


Figure 8. Same as Figure 7 but for CO. The removal of any one shielding component tends to strongly depress the global CO fractions.

Table 2. Model results.

Model Name	Mass fraction ¹		$M_{\text{H}_2}/M_{\text{tot}}^2$	$M_{\text{CO}}/M_{\text{C,tot}}$	$M_{\text{H}_2}/M_{\text{H}_2,\text{fid}}$	$M_{\text{CO}}/M_{\text{CO,fid}}$	$\text{Err}_{\text{H}_2}^3$	Err_{CO}^3
	$f_{\text{H}_2} > 0.5$	$f_{\text{CO}} > 0.5$						
Fiducial								
F1	.194 / 1	.325(-2) / .115	.150	.922(-2)	1	1	0	0
F2	.152 / 1	.348(-2) / .108	.125	.916(-2)
F3	.103 / 1	.100(-2) / .600(-1)	.862(-1)	.459(-2)
Variation								
V1	.185 / 1	.386(-2) / .136	.157	.110(-1)	1.05	1.19	.150	.146
V2	.166 / 1	.332(-2) / .118	.138	.920(-2)	.922	.998	.830(-1)	.279(-1)
V3	.387(-2) / .137	.254(-3) / .900(-2)	.345(-2)	.113(-2)	.233(-1)	.119	.739	.826
V4	.387(-2) / .137	.949(-3) / .335(-1)	.337(-2)	.803(-2)	.225(-1)	.871	.739	.587
V5	.151 / 1	.456(-3) / .163(-1)	.138	.282(-2)	.920	.306	.142	.718
V6	.896(-1) / 1	.0 / .0	.858(-1)	.414(-3)	.572	.450(-1)	.429	.913
V7	.661(-1) / 1	.713(-3) / .254(-1)	.540(-1)	.327(-2)	.360	.355	.562	.663
V8	.343 / 1	.598(-2) / .182	.253	.544(-1)	1.69	2.53	.696	2.10
V9	.100 / 1	.0 / .0	.971(-1)	.782(-3)	.647	.848(-1)	.353	3.17
V10	.0 / .0	.0 / .0	.166(-4)	.285(-5)	.111(-3)	.308(-3)
Temperature								
T1	.193 / 1	.580(-2) / .204	.151	.120(-1)	1.01	1.31	.197(-1)	.446
T2	.0 / .0	.0 / .0	.160(-4)	.295(-5)	.112(-3)	.320(-3)
T3	.691(-1) / 1	.713(-3) / .251(-1)	.567(-1)	.289(-2)	.377	.313	.549	.634
T4	.416 / 1	.115(-1) / .407	.298	.253(-1)	1.99	2.74	.982	1.89
Local								
L1	.260 / 1	.750(-2) / .144	.209	.188(-1)	1.39	2.04	.390	1.11
L1a	.235 / 1	.410(-2) / .140	.182	.105(-1)	1.21	1.14	.221	.205
L2	.563(-1) / .983	.651(-5) / .0	.532(-1)	.117(-3)	.350	.124(-1)	.617	.975
L3	.131 / 1	.648(-2) / .202	.107	.167(-1)	.717	1.74	.305	.876
L4	.250 / 1	.413(-2) / .140	.198	.106(-1)	1.32	1.15	.316	.223
L5	.914(-1) / 1	.402(-2) / .141	.785(-1)	.820(-2)	.528	.891	.459	.257
L6	.212 / 1	.449(-2) / .158	.166	.123(-1)	1.11	1.34	.110	.335

Notes — Numbers in parenthesis represent the scientific notation exponent, i.e., $0.19(-3) \equiv 0.19 \times 10^{-3}$. (1) The total gas mass fraction with an H₂ (first column) or CO (second column) fraction greater than 0.5. The second number, after the slash, is the equivalent quantity when only considering cold, dense gas ($n_{\text{H}} > 100 \text{ cm}^{-3}$, $T < 100 \text{ K}$). (2) The total mass in the fiducial simulation (F1) is $4.57 \times 10^4 M_{\odot}$. (3) See text surrounding Equation 34 for the description of the H₂ and CO error measurements.

terminated radiative shielding models presented in Section 3.4 (via Equation 29).

3.2 Variations on the fiducial models: V1-V10

To model the spatial distribution of FUV emissivity (as required by Equation 25) we treat massive OB stars as the primary emitters of FUV radiation whose vertical density obeys the functional form of Equation 14. The fiducial model F1 utilized a vertical scale height of $H = 100 \text{ pc}$, roughly consistent with the measured mean half-width of H₂ in the inner Galaxy of $\simeq 59 \text{ pc}$ (Bronfman et al. 2000). Models V1 and V2, which use scale heights of $H = 20$ and 200 pc , respectively, demonstrate the relatively insensitivity of our results to H . Inspecting Table 2, model V1 has 5% more H₂ and $\approx 20\%$ more CO than F1, reasonable considering that a reduction (increase) in H lowers (increases) the overall global number of FUV photodissociating photons. Model V2 has a corresponding decrease in amount of H₂, though less than a 1% reduction in the total CO mass as compared with F1. Morphologically, models V1 and V2 are virtually indistinguishable from F1.

Models V3 through V6, in which one or a number of shielding mechanisms are artificially switched off, are designed to assess the relative importance of self- and dust-shielding in determining the

molecular abundances. Unsurprisingly, each of these models results in overall less H₂ and CO mass than the comparison model F1. Models V3, V4, V5, V6 have, respectively, 2.3, 2.3, 92, and 57% the mass of H₂ as model F1. As for the CO mass, these percentages become 12, 87, 30, and 4.5% (Table 2).

Figures 7 and 8 show mass-weighted projections of the H₂ and CO fractions for models F1, V3, V4, V5, and V6. A comparison of models F1 with V3 and V4 in Figure 7 highlights the importance of H₂ self-shielding in attenuating the ISRF and reducing the H₂ photodissociation rate. The H₂ fractions in models V3 and V4, which do not include H₂ self-shielding (Equation 17; $f_{\text{self,H}_2} = 1$), are substantially suppressed (by nearly a factor of 50 — see Table 2) compared with models that do include self-shielding. In these models, H₂ fractions of unity are only realized in the highest density gas that approaches the resolution of this study. Switching off CO self- and cross-shielding, model V5, unsurprisingly has no effect on the H₂ abundance.

In model V6 dust shielding is deactivated in an effort to isolate its role in reducing the direct photodissociation rates of H₂ and CO. Importantly, dust shielding remains active for all other species besides H₂ and CO. This choice removes the indirect effect that increased photodissociation rates for other chemical species would have in altering the chemical formation pathways of CO and, to a

much lesser extent, H_2 . As shown in the far right panel of Figure 7, the removal of dust shielding has a fairly small, though non-zero, effect on the H_2 fraction.

In contrast to H_2 , self-shielding, cross-shielding by H_2 ¹, and dust shielding are all comparably important in photoshielding CO molecules. This can be seen in Figure 8 where each model results in a significant decrease in the amount of CO as compared with model F1. Model V4, in which H_2 self-shielding is switched-off and the global H_2 fractions are significantly reduced, demonstrates the importance of H_2 shielding CO via their overlapping photodissociation lines in the Lyman-Werner bands. Models V5 and V6, meanwhile, respectively underscore the importance of self- and dust shielding. However, the inclusion of *any* form of radiative shielding, whether from self-, cross-, or dust-shielding, results in the formation of gas with $f_{\text{CO}} \approx 1$ at the highest densities, $n \sim 10^3 \text{ cm}^{-3}$. Model V10 (not shown), in which all radiative shielding is turned off, results in no gas with $f_{\text{CO}} > 10^{-4}$, a statement that additionally applies to H_2 .

We can explore this further by examining the cumulative distribution functions (CDF) of f_{H_2} and f_{CO} for models V3-V6 and F1, which we plot in Figure 9. Here, we restrict this analysis to cold, dense gas as this makes for a more potent demonstration of the competing factors at work; qualitatively identical conclusions would be drawn from the CDFs that included all gas. Focusing first on H_2 (left panels), we see the removal of dust shielding only reduces the gas fraction with $f_{\text{H}_2} \gtrsim 0.9$ as compared with model F1. Turning off H_2 self-shielding (models V3 and V4), conversely, suppresses the H_2 mass $\sim 10 - 50\%$ for gas with $f_{\text{H}_2} \gtrsim 0.1$. Here it is clear that by and large the dominant mechanism by which H_2 is shielded from the FUV ISRF is self-shielding, at least for the range of ISRF properties probed in these simulations. In the analytic models of Krumholz et al. (2008), the relative importance of self-shielding and dust shielding depends on the value of χ , Equation 33. At Milky Way values of χ the two processes are about equally important, but as noted above, the simulations we analyze here have radiation field intensities that are $\sim 2 - 5$ times smaller than those found in the Solar neighborhood, so the relative dominance of self-shielding is not surprising.

As for CO, a great deal of information can be extracted from a comparison of the various CDFs, shown in the right panels of Figure 9. Model V4 does not include H_2 self-shielding ($f_{\text{self},\text{H}_2} = 1$) and as a consequence has a highly suppressed H_2 fraction. This choice encapsulates two combined effects, one chemical and one radiative, both of which act to decrease the amount of CO. First, $f_{\text{CO},\text{H}_2}(N_{\text{H}_2})$ (the cross-shielding factor) is reduced as the global H_2 column densities are significantly reduced. Second, the two predominant CO formation pathways (one involving OH, and the other CH) both rely on the availability of H_2 , thus reducing the overall speed of the chemical formation pathways that lead to CO. These effects combined result in the CO mass being suppressed by a factor of $\sim 5 - 10$ for $f_{\text{CO}} \gtrsim 10^{-3}$ compared with model F1 — the suppression increases with increasing CO fraction. From this model alone, however, is it unclear which of these two effects, chemical or radiative, is dominant.

Model V5 does not include CO self-shielding nor cross-shielding from H_2 . As can be seen, this has little effect in gas with a low CO fraction ($f_{\text{CO}} < 10^{-3}$). Evidently for this 'diffuse' CO

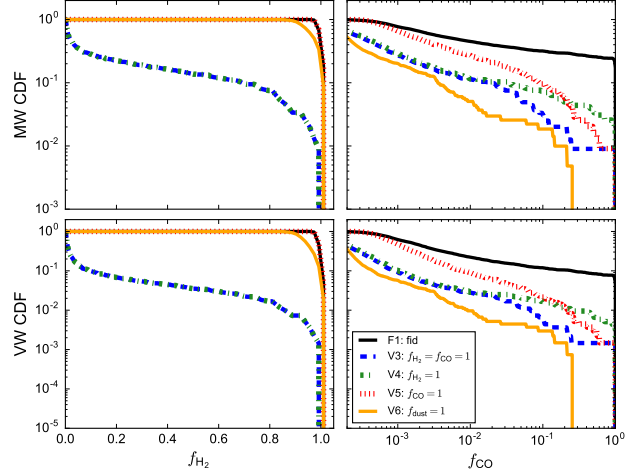


Figure 9. Mass weighted (top row) and volume weighted (bottom row) cumulative distribution functions (CDFs) of the H_2 (left panels) and CO fraction (right panels). This analysis is restricted to cold, dense gas ($n_{\text{H}} > 100 \text{ cm}^{-3}$, $T < 100 \text{ K}$). Lines of different color denote models with different treatments of dust- and self-shielding as described in the text.

gas, CO self-shielding and H_2 cross-shielding is relatively unimportant. For CO rich gas ($f_{\text{CO}} \gtrsim 0.5$), the mass in CO is suppressed by a factor of 20. Chemically, there is no suppression of the H_2 abundance in this model so any reduction in f_{CO} is entirely due to the lack of shielding from itself and H_2 .

The drop in the CO fraction between models V5 and V3 is a chemical, not radiative, effect and highlights the role of H_2 in the CO formation pathways. Observe that the sole difference between models V5 and V3 is that the H_2 fraction in model V3 is highly suppressed due to the lack of H_2 self-shielding. With regards to CO, this isolates the effect that the H_2 abundance has on the efficiency of the chemical pathways that lead to CO. Quantitatively, this purely chemical effect reduces the total CO mass by $\approx 60\%$ (see Table 2). Furthermore, at the highest CO fractions, there is no difference between model V5 and V3 in terms of the CDF, while model V4 still displays a roughly order-of-magnitude drop. This implies that a reduction in the H_2 fraction (via removing H_2 self-shielding) decreases the CO fraction predominantly through less H_2 cross-shielding and a larger CO photodissociation rate, as opposed to a reduction in the CO formation rate.

The CO fractions realized in the absence of dust shielding (model V6) are similar to that of models V3 and V4 for $f_{\text{CO}} \lesssim 10^{-3}$, underscoring the importance of dust shielding for CO. In other words, the consequence of removing dust shielding for CO is roughly comparable to the combined removal of CO self-shielding, H_2 cross-shielding, and decreased CO formation efficiency due to a suppressed H_2 abundance. Evidently, dust shielding is critical for the formation of CO fractions approaching unity. In the absence of dust shielding, no gas is able to form with $f_{\text{CO}} > 0.3$.

Models V7 and V8 consider the scenario where the overall strength of the FUV radiative intensity is, respectively, increased or decreased by a factor of 10. Increasing the ISRF by a factor of 10 (V7) results in a $\approx 2.7\times$ decrease in both the total H_2 and CO mass, while decreasing the radiative intensity tenfold (V8) results in a factor of 1.69 more H_2 and 2.53 times more CO mass.

¹ The CO abundance decreases with diminishing H_2 , though whether this stems from H_2 cross-shielding or reduced CO formation rates is a subtle issue we explore later in this section

In model V9, the cosmic-ray ionization rate is increased from $\zeta = 10^{-17}$ to 10^{-16} s^{-1} to gauge its impact on molecular chemistry. This has a much more severe effect on the CO abundance than the H_2 abundance. As seen in Table 2, increasing ζ reduced the global H_2 mass by roughly a factor of 2, while the CO mass fell to roughly 8% its value in model F1. This strong dependence of the CO abundance on the cosmic ray ionization rate is an indirect effect, stemming mainly from the cosmic ray ionization of neutral Helium and the subsequent charge-exchange destructive reaction between He^+ and CO.

Finally, in model V10, all radiative shielding is switched off, causing a catastrophic decrease in the abundances of H_2 and CO. As can be seen in Table 2, this results in zero gas with an H_2 or CO fraction higher than 0.5. The total molecular mass is also significantly reduced; the total mass of H_2 and CO is 0.01% and 0.03%, respectively, as compared to model F1. This result only underscores the importance of radiative shielding in permitting the formation of significant molecular abundances. However, as will be shown in Section 3.3, the removal of all radiative shielding has a relatively small effect on the temperature structure of the gas.

3.3 Temperature evolution: T1-T4

In models T1-T4, the gas temperature is evolved to equilibrium along with the chemical abundances, utilizing the thermal processes described in Section 2.3. Model T1 is identical to model F1 save for the temperature evolution, while model T2 operates under optically thin conditions, i.e., no radiative shielding. In models T3 and T4 the mean FUV intensity is altered, though are otherwise identical to model T1.

In Figure 10 we show density-temperature diagrams for models F1 (whose density and temperature are unchanged from the values initially supplied by K15), T1, T2, T3, and T4. At any given density, the spread in temperature for model T1 is significantly reduced as compared with model F1. In fact, any spread in temperature in model T1, at a given density, is overwhelmingly due to spatial variations in the photoelectric heating rate (Equation 8) which arises due to differences in the degree of radiative shielding (via A_v) and the vertical dependence of the FUV emissivity (Equation 14) and consequently the unattenuated radiation field G_0 . Aside from this reduction in the temperature spread, the density-temperature relationship between models F1 and T1 agree remarkably well below a density of $\sim 100 \text{ cm}^{-3}$. Above $n_{\text{H}} = 10^2 \text{ cm}^{-3}$, the temperature in model T1 begins to drop below that of F1, reaching $\approx 5 \text{ K}$ by 10^3 cm^{-3} as a result of CO line emission, a cooling pathway not included in K15.

The relationship between density and temperature in Model T2, which does not include the effect of radiative shielding, is similar to that of model T1 below $n_{\text{H}} = 100 \text{ cm}^{-3}$. The only significant difference between the two models is the absence of $< 10 \text{ K}$ degree gas at the highest densities, due to the complete lack of any significant CO cooling, in model T2. Even by increasing the midplane G_0 by a factor of 10 to $G_{0,\text{midplane}} = 3.6$ (model T3), a cold phase still develops, though at a slightly larger density and equilibrium temperature of 70 K before CO cooling cools the gas below $\sim 10 \text{ K}$. Model T4, with its tenfold reduction in the strength of the midplane FUV intensity, exhibits the emergence of a molecular cold phase at the relatively low density of $\sim 0.1 \text{ cm}^{-3}$. The molecular nature of this cold phase should be viewed as an artifact of our equilibrium assumption, given the chemical time at $n_{\text{H}} = 0.1 \text{ cm}^{-3}$ is of order 10 Gyr — see Section 4. The minimum temperature obtained in model T4 is also lower than any other model, nearly

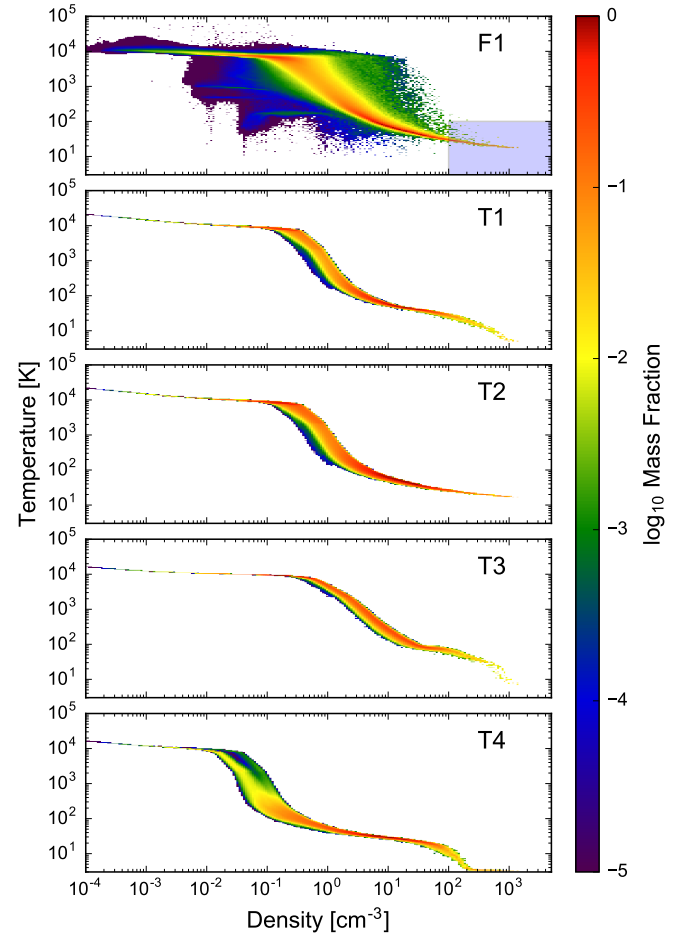


Figure 10. Density-temperature phase diagrams for the fiducial model F1 (top), T1, T2, T3, and T4. In models T1-T4, temperature is evolved along with the chemical abundances. The density-temperature relationship of model F1, where the temperature is not evolved, is unchanged by our analysis and identical to that originally supplied by the simulation of K15. The temperature spread in model T2, mainly present at temperatures $30 \text{ K} < T < 10^4 \text{ K}$ is entirely due to the vertical dependence of the unattenuated radiation field. The primary effect of changing the FUV intensity (models T3 and T4) is a shift in the density at which gas transitions from the warm to cold neutral medium. The blue shaded region in the top panel denotes this paper’s definition of cold, dense gas.

reaching the cosmic microwave background (CMB) temperature floor ($T_{\text{CMB}} = 2.725 \text{ K}$) around $n_{\text{H}} \approx 2 \times 10^2 \text{ cm}^{-3}$. While radiative shielding is crucial for the formation of significant molecule fractions (Section 3.2) and for reaching the lowest temperatures observed in the ISM, the ubiquitous appearance of a marginally cold phase (where $T \lesssim 100 \text{ K}$) in all these models supports the important point that shielding is not strictly required for the transition to a cold phase, at least in the regime where the background FUV radiation field strength is relatively modest, $G_0 \lesssim 1$.

3.4 Local approximations for radiative shielding: L1-L6

The primary objective in this section is to assess the validity and accuracy of utilizing a locally computed shielding length to model radiative attenuation and thus the FUV-radiation regulated chemical state. We will do this by examining how closely the local models

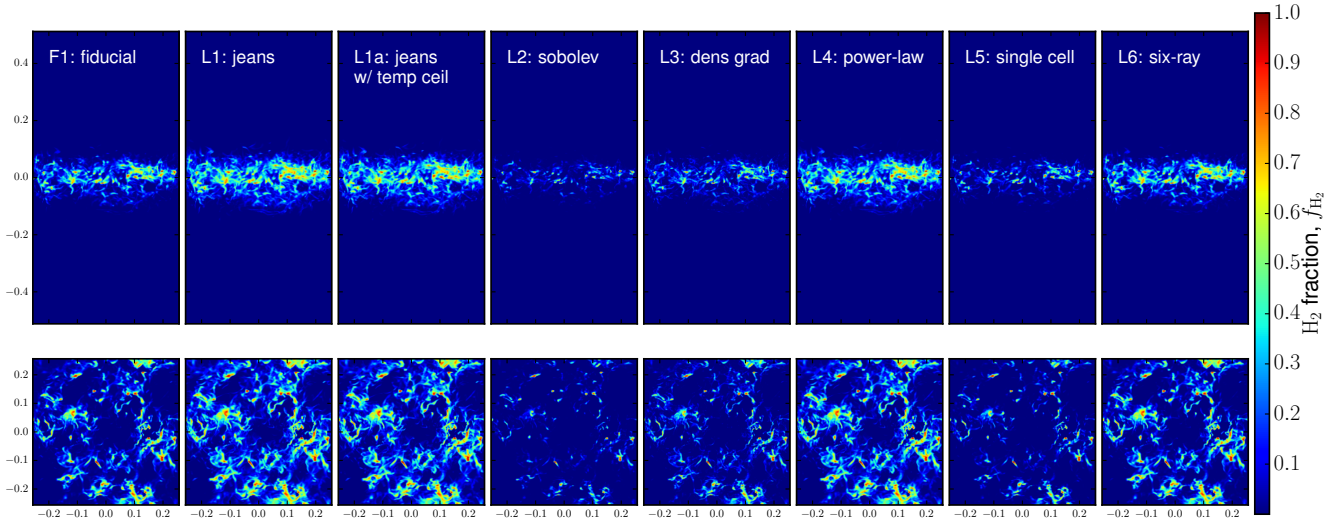


Figure 11. Mass weighted projections of f_{H_2} for models with different locally computed approximations for the shielding length L_{shield} .

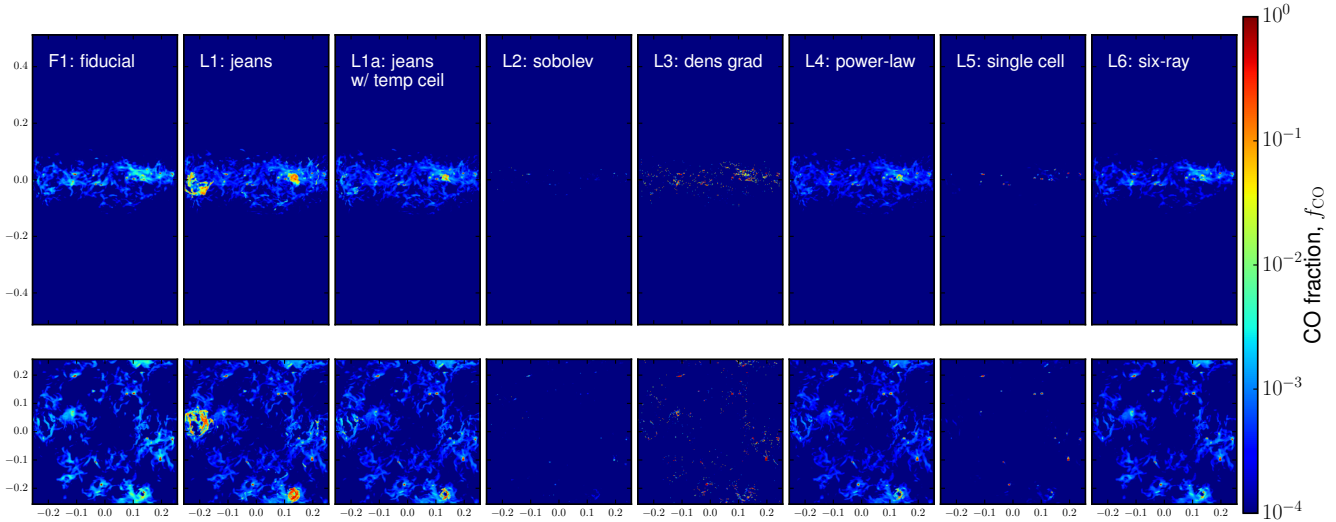


Figure 12. Same as Figure 11 but for CO.

L1-L6 reproduce the H_2 and CO abundances of the fiducial model F1 using a variety of qualitative and quantitative measures. Considering first the total mass of H_2 (M_{H_2} , Table 2 column 6), we see all the local models come within a factor of 2 of F1, with the exception of model L2 (Sobolev approximation) which results in 65% less H_2 . The total mass of CO is a bit more scattered than M_{H_2} , though the four best performing local models (L1a, L3, L4, and L6) have M_{CO} within 35% of model F1’s value. Any given local approximation model always produces an increase (or decrease) between both the total H_2 and CO masses, with the exception of model L3 (density gradient) which, due to the peculiarity of using density gradients to estimate a global column density, results in $\approx 30\%$ less H_2 , and nearly 75% more CO, than model F1.

The morphology and distribution of H_2 between models L1-L6 and F1 (Figure 11) highlights the relative similarity between the distribution of molecular hydrogen in many of the local approximation models compared with the fiducial model. Evidently the exact

prescription used to account for the attenuation of the ISRF is a relatively unimportant factor in modeling the overall distribution of H_2 gas. The inclusion of *some* form of radiative shielding, however, is a necessary ingredient to form any significant H_2 fraction — not shown here is model V10 (no shielding) in which no cell of gas achieves an H_2 (or CO) fraction greater than 10^{-3} and results in a factor $\sim 10^{-4}$ less H_2 and CO mass.

It is important, however, to scrutinize any variation between the various local models and model F1 in Figure 11. Models in which radiative shielding is based on the local Jeans length (L1 and L1a) or a power-law fit between n_{H} and $A_{\text{V,eff}}$ (L4) appear to slightly overestimate the H_2 fraction, while a shielding length computed via the velocity divergence (Sobolev length; L2), the density gradient (L3), or a single computational cell (L5), tend to underpredict f_{H_2} . By eye, the best level of agreement is achieved by the six-ray approximation (model L6); this is not a strictly a local approximation, but is instead effectively the result of reducing the

number of ray-tracing propagation directions from 48 to 6, now all aligned along the cartesian axes.

In contrast to H_2 , the spatial distribution and amount of CO (Figure 12) shows a great deal more sensitivity to the radiative shielding prescription. As compared with model F1, models L2 and L5 fail to produce any gas with visually discernible CO. In model L3 there exists what appears to be an unphysical scattering of cells with f_{CO} approaching unity and a paucity of diffuse CO, $10^{-4} < f_{\text{CO}} < 0.1$. As with H_2 , the six-ray approximation (model L6) appears to do the best job in reproducing f_{CO} . It should be noted, though, that large concentrations of CO can be difficult to discern given the small spatial extent of these concentrations.

Model L1, where $L_{\text{shield}} = L_J$, seems to perform reasonably well in matching f_{CO} from model F1, except for the appearance of two large (~ 50 pc) structures with $f_{\text{CO}} > 0.1$ that do not exist in model F1. We attribute this to out-of-equilibrium hot gas with density $n_{\text{H}} \gtrsim 1 \text{ cm}^{-3}$ and temperature $T \gtrsim 100$ K. Since the Jeans length $L_J \propto T^{1/2}$, these cells have an unphysical elevated shielding length which reduces the FUV radiation intensity and boosts the CO abundance. This is an undesired effect of modeling L_{shield} with L_J — these cells do not represent gravitationally collapsing cores and physically should not experience a higher degree of radiative shielding. This shortcoming can be addressed quite simply, however, by introducing a temperature ceiling into the calculation of L_J . In model L1a the shielding length is given by this temperature capped Jeans length with an empirically chosen ceiling temperature of $T_{\text{ceiling}} = 40$ K. An inspection of Figure 12 confirms that these unphysical CO rich bubbles are strongly suppressed in model L1a.

To better understand the relationship amongst the local models, in Figure 13 we plot the mass-weighted effective extinction (Equation 30) as a function of density for each local model as compared with model F1 (previously plotted in Figure 6). Here it is clear how well models L1, L1a, L4, and L6 perform in matching the effective visual extinction as computed from detailed ray-tracing, at least at high densities, $n_{\text{H}} > 10 \text{ cm}^{-3}$. Models based on local derivatives of grid-based quantities severely overpredict (L3) or underpredict (L2) the true column density. Caution should be used in interpreting Figure 13; in doing so, one would be led to conclude that model L4 should be the best performing local model since it was explicitly calibrated to match the $A_{\text{V,eff}} - n_{\text{H}}$ relationship from model F1. As discussed in Section 3.2, H_2 is primarily shielded by itself, the degree of which is a function of the H_2 column density N_{H_2} , not N_{H} . Thus the $n_{\text{H}} - A_{\text{V,eff}}$ relationship is not the ideal proxy for how well a model will predict the H_2 abundance.

It is important to have a single number that characterizes the level of agreement, with regards to the spatial distribution of H_2 and CO, between each local approximation model and the fiducial model F1. Many such quantitative metrics could be constructed which effectively compress a three-dimensional error distribution to a single value. For our purposes here, we favor such a metric that represents the ability of a local approximation to accurately model the atomic-to-molecular transition for both H_2 and CO, rather than one that is sensitive to diffuse molecules and low density gas, since this is most relevant in regards to both observations and molecule-mediated thermo-energetics. To this end, we have found the best metric to be the mass-weighted fractional error of $\Delta\rho_x/\rho_x$ which can be expressed as

$$\text{Err}_x = \frac{\sum_{i,j,k} \left| \frac{\Delta\rho_x}{\rho_{x,\text{fid}}} \right| \rho_{x,\text{fid}}}{\sum_{i,j,k} \rho_{x,\text{fid}}} = \frac{\sum_{i,j,k} |\Delta\rho_x|}{\sum_{i,j,k} \rho_{x,\text{fid}}} \quad (34)$$

where $\Delta\rho_x = \rho_{x,\text{fid}} - \rho_{x,\text{approx}}$, $\rho_{x,\text{fid}} = \rho_{x,\text{fid}}(i, j, k)$ is the

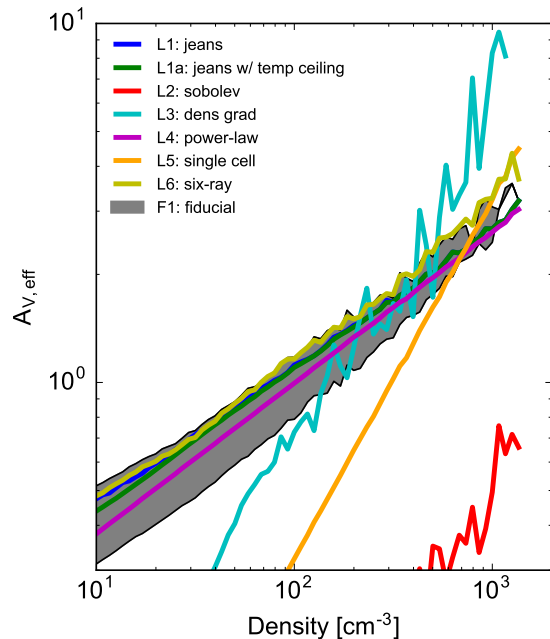


Figure 13. Mass-weighted effective visual extinction ($A_{\text{V,eff}}$, Equation 30) vs. density. Lines of different color denote models with different treatments of radiative shielding (models L1-L6) while the black shaded region represents the $1\text{-}\sigma$ dispersion of $A_{\text{V,eff}}$ for model F1.

density of molecule x in model F1, $\rho_{x,\text{approx}} = \rho_{x,\text{approx}}(i, j, k)$ is the density of molecule x in any separate model, x denotes either H_2 or CO, and the sum runs over all cells (i, j, k) . Equation 34 is formulated such that perfect agreement between the molecular abundances would produce $\text{Err}_x = 0$, while $\text{Err}_x = 1$ signifies the local approximation model formed no molecules of species x whatsoever. To prevent extremely small, negligible abundances from skewing this error metric and to better quantify the significant differences amongst the local models, we omit cells with concentrations so low where CO would not be a significant coolant, adopting a value of 10^{-2} for both CO and H_2 . We compute the above error metric between model F1 and each other model (see Table 1) except for F2 and F3, whose different density maps make this error metric meaningless.

An examination of Table 2 shows that, amongst the local models, the six-ray approximation possesses the smallest H_2 weighted error (L6, $\text{Err}_{\text{H}_2} = 0.11$), followed by the temperature capped-Jeans length (L1a, 0.221) and density gradient (L3, 0.305). As for CO, model L1a has the lowest error ($\text{Err}_{\text{CO}} = 0.205$) followed by the power-law fit (L4, 0.223) and single cell shielding (L5, 0.257). This error metric does have limitations, and should be considered along with the other comparison measures. For instance, the relatively low Err_{CO} value of model L5 would suggest it does an excellent job matching the CO abundances of F1, though inspecting its CO spatial distribution (Figure 12; see also Figure 15) suggests otherwise. This discrepancy is due to the CO error metric (Err_{CO} , Equation 34) being weighted by f_{CO} , while the logarithmically scaled projections allow the detection of much more diffuse ($f_{\text{CO}} \sim 10^{-3} - 10^{-2}$) CO.

As a final comparison between models L1-L6 and F1, we show cell-by-cell, mass-weighted abundance comparisons of H_2 and CO in Figures 14 and 15. These plots are generated by comparing the H_2 fraction between model F1 ($f_{\text{H}_2,\text{fid}}$) and each local

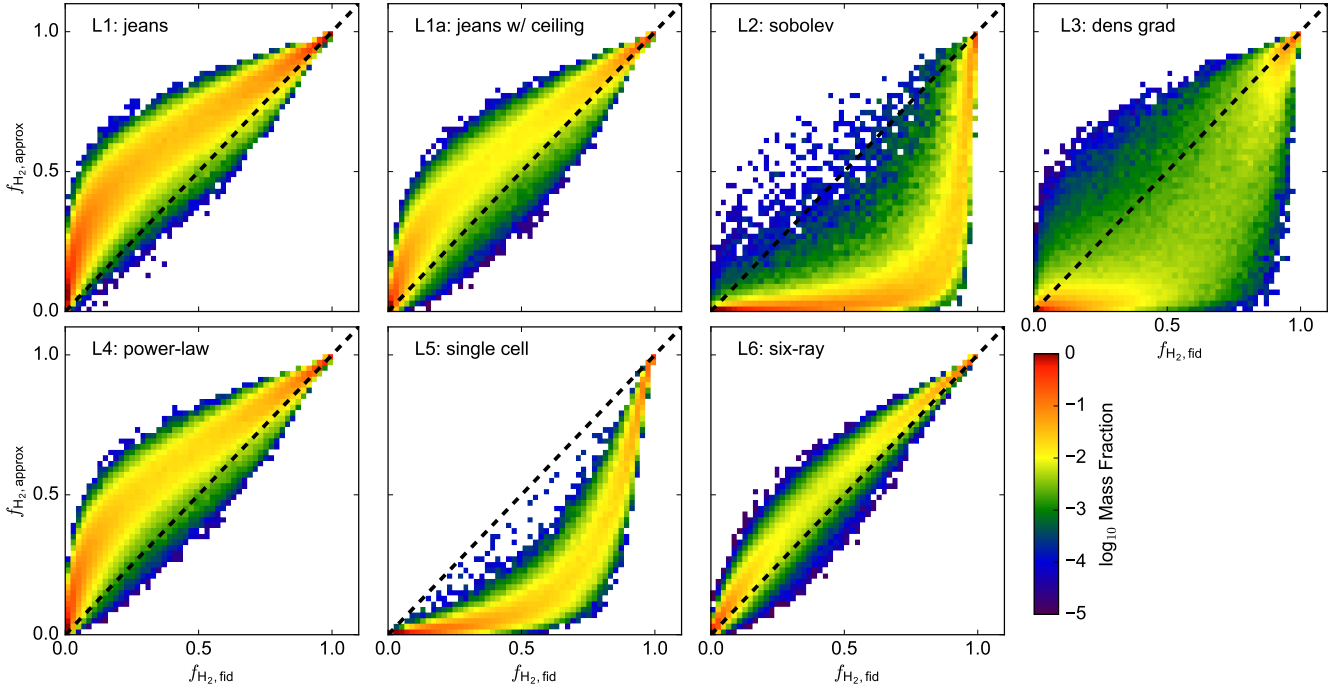


Figure 14. Cell-by-cell, mass-weighted abundance comparisons between each local model (L1-L6) and the fiducial model F1. These plots are generated by comparing the H₂ fraction between model F1 ($f_{\text{H}_2,\text{fid}}$) and each local model ($f_{\text{H}_2,\text{approx}}$) on a cell-by-cell basis. The color scale here represents the logarithm of the mass fraction in a particular region of the $f_{\text{H}_2,\text{fid}} - f_{\text{H}_2,\text{approx}}$ phase space. Perfect agreement between a local model and model F1 would exclusively lie on the diagonal dashed line defined by $f_{\text{fid}} = f_{\text{approx}}$. Given f_{H_2} is expressed on a linear scale, the level of agreement between the local and ray-trace models is quite good, with the largest discrepancy seen in model L2 which tends to underpredict the H₂ abundance by a factor of ~ 5 .

model ($f_{\text{H}_2,\text{approx}}$) on a cell-by-cell basis (and similarly for CO). The color scale represents the mass fraction in a particular region of the $f_{\text{fid}} - f_{\text{approx}}$ phase space. Perfect agreement between a local model and model F1 would exclusively lie on the diagonal dashed line defined by $f_{\text{fid}} = f_{\text{approx}}$.

Local models based on the Jeans length (L1, L1a) or a power-law fit (L4) tend to slightly overpredict the H₂ abundance by $\sim 20-30\%$ (see Table 2). As expected, when all radiative shielding is assumed to take place in the immediate vicinity of a computational cell (model L5) the H₂ abundance is slightly underpredicted by roughly a factor of 2. Models in which the local shielding length requires a computation of a discrete gradient or divergence of a grid variable (L2 and L3) tend to exhibit a larger degree of scatter in the H₂ abundance as compared to other local models (Figure 14). As before, model L6 performs the best in matching the results of the fiducial model, overpredicting the total H₂ mass by only 11%.

Turning to CO (Figure 15), we see a much larger scatter and discrepancy amongst the local models. Models L1 and L3 tend to significantly overpredict the CO abundance by up to four orders of magnitude. Comparing models L1 and L1a, however, shows how effectively this disagreement can be greatly reduced by imposing a temperature ceiling of $T = 40$ K in the calculation of the Jeans, and thus shielding, length. Model L2 is unique in that effectively no gas exists with $f_{\text{CO}} > 0.1$. Single cell radiative shielding (model L5) results in relatively little scatter but an underprediction of the CO fraction in all cells save for those with CO fractions approaching unity. Model L5 and L1a also have a lower Err_{CO} (1D error representation) than model L6, though the 2D error distribution displayed in Figure 15 seems to suggest L6 to be better performing than L5 and on-par with model L1a, highlighting the utility of mul-

iple error comparisons to gauge the effectiveness of each model in reproducing the molecular abundances of the fiducial model.

Finally, it is interesting to note the similarity between models L1a (Jeans with temperature ceiling) and L4 (power-law fit) in their prediction of both the H₂ and CO abundances. This can be attributed to their respective density scalings: Model L4 utilizes a $A_{\text{v,eff}} - n_{\text{H}}$ relationship calibrated from model F1 ($A_{\text{v,eff}} \propto n_{\text{H}}^{0.42}$), while the Jeans length approximation can be shown to obey a $A_{\text{v,eff}} \propto n_{\text{H}}^{1/2}$ scaling. The similarity of these exponents should be unsurprising, though, given the physical principle underlying the Jeans length: L_{J} is the appropriate shielding length to utilize when radiative shielding is due to surrounding material in a dense clump undergoing gravitational instability, exactly the physical entities that are able to achieve $f_{\text{H}_2} > 0.1$ and $f_{\text{CO}} > 10^{-4}$ in the simulations we analyze here.

4 DISCUSSION AND CONCLUSIONS

In this paper we have applied ray-tracing and chemical network integration to static simulation snapshots in an effort to model the distribution, morphology, and amount of H₂ and CO gas in a finite, but representative, portion of a galactic disk. We have additionally performed calculations where local approximations, instead of ray-tracing, were employed to account for radiative shielding in an effort to assess the validity and accuracy of such radiative transfer alternatives.

We find significant concentrations of H₂ gas ($f_{\text{H}_2} > 0.1$) are vertically restricted to within ≈ 80 pc of the galactic midplane and possess a filamentary morphology which traces that of the un-

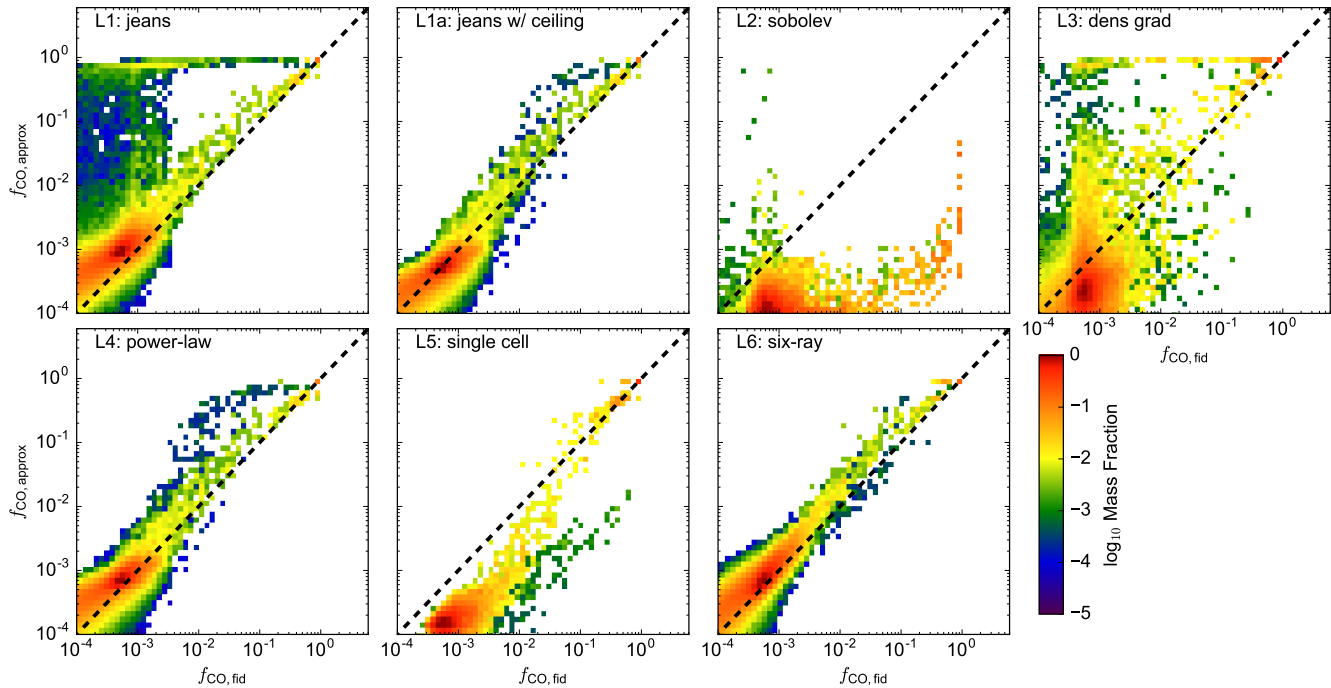


Figure 15. Same as figure 14, but for CO and plotted on a logarithmic scale. As compared with H₂, larger discrepancies and scatters are seen when comparing the local models f_{CO} versus model F1. The Sobolev approximation (model L2) is unique in that effectively no gas exists with $f_{\text{CO}} > 0.1$. Aside from model L2, models L1 and L3 result in the largest scatters as compared with F1, in the sense that they have the capability to significantly overpredict the CO fraction. For model L1, this scatter can be effectively eliminated by imposing a temperature ceiling in the calculation of the Jeans length (model L1a).

derlying gas distribution. Gas with significant CO concentrations ($f_{\text{CO}} > 0.1$) is further confined to only the highest density clumps, located interior to H₂ rich gas. Radiative shielding is crucial for the development of any gas with an H₂ or CO fraction $> 10^{-3}$. When the gas temperature is permitted to reach equilibrium along with the chemical abundances, we find little change from the K15 temperature values (except for gas at the highest densities, $n \gtrsim 10^2 \text{ cm}^{-3}$, where CO cooling became effective), suggesting the bulk of the gas in K15 to exist in thermal equilibrium, and an overall insensitivity of temperature to radiative shielding.

Different physical mechanisms are responsible for the radiative shielding of H₂ and CO. For H₂, self-shielding is far dominant over dust shielding in reducing the H₂ photodissociation rate in all regimes explored here. The dominant shielding mechanisms for CO, on the other hand, are regime dependent. More diffuse CO ($f_{\text{CO}} \lesssim 10^{-2}$) is shielded primarily by dust and H₂ while CO rich gas ($f_{\text{CO}} > 0.1$) additionally depends on the presence of self-shielding by the molecule itself. However, this regime dependence for CO shielding may be sensitive to the large-scale gas distribution in this particular simulation.

We have compared a number of commonly used local approximations for radiative shielding to ray-tracing based solutions of the radiative transfer equation. Overall, it is promising how well many of the local models reproduce the H₂ and CO abundances as compared with a more accurate ray-tracing based approach. One of the main objectives of this work is to inform multidimensional simulations as the validity of these local approximations to account for FUV radiative shielding. Based on our analysis, the six-ray approximation (L6), temperature-capped Jeans length (L1a), and power-law (L4) perform the best in matching the H₂ and CO abundances of model F1.

Among the approximations where the effective shielding length for a given cell (or, potentially, SPH particle) is exclusively computed from *local* quantities (thus excluding model L6), the temperature-capped (at $T = 40 \text{ K}$) Jeans length performed the best, an assessment based on its superiority in terms of matching the total H₂ and CO masses of model F1, and possessing the smallest H₂ and CO weighted errors (Equation 34). We caution, however, that we have only explored one regime, that of a turbulent galactic disk, with relatively coarse (2 pc) resolution. While this regime does include both the H I-H₂ and, at the highest densities, C II-CO atomic-to-molecular transitions, there are undoubtedly physical environments to which this analysis applies poorly.

Furthermore, the use of any such an approximation for L_{shield} critically depends on the physics a multidimensional simulation is attempting to probe. If one simply wishes to model the thermal impact of the H I-H₂ and C II-CO transitions, then coarse approximations, like those discussed above, are likely physically appropriate. On the other hand, we do not recommend such simple approximations when, for example, attempting to reproduce the detailed distribution and concentration of a large number of chemical species for observational comparison. In these cases, performing detailed, multi-frequency radiative transfer in post-processing, or utilizing advanced radiative transfer modules that operate on-the-fly, is a much more appropriate approach.

All the models presented here operate under the assumption of steady-state (equilibrium) chemistry, the validity of which can be assessed by comparing the chemical and dynamical timescales. Taking $\mathcal{R} \approx 3.0 \times 10^{-17} \text{ cm}^3 \text{ s}^{-1}$ to be the rate coefficient for H₂ formation on grain surfaces, and $\mathcal{C} \equiv \langle n_{\text{H}}^2 \rangle / \langle n_{\text{H}} \rangle^2$ to be the gas clumping factor on unresolved scales, the chemical time, the timescale for fully atomic gas to convert to molecu-

lar form, is given by $t_{\text{chem}} \approx (n_{\text{H}} \mathcal{R} \mathcal{C})^{-1} \approx 10^3 n_{\text{H}}^{-1} \mathcal{C}^{-1}$ Myr. The dynamical time, roughly the timescale for turbulent motions to displace molecular gas, can be expressed as $t_{\text{dyn}} \approx 1 \text{ Myr} (L/\text{pc})^{1/2}$, which assumes a linewidth-size relation $v_{\text{turb}} \approx 1 \text{ km s}^{-1} (L/\text{pc})^{1/2}$ (Dobbs et al. 2014). The assumption of equilibrium is violated when $t_{\text{dyn}} < t_{\text{chem}}$, or equivalently when $n_{\text{H}} \lesssim 10^2 \text{ cm}^{-3} (L/\text{pc})^{-1/2} (\mathcal{C}/10)^{-1}$. Thus the equilibrium chemistry is reasonably justified given we focus our analysis on H_2 within the high density H I- H_2 transition. Non-equilibrium effects, however, are likely important at lower densities where the H_2 formation timescale is much longer. This back-of-the-envelope argument, though, should be compared with actual findings from multi-dimensional simulations that included non-equilibrium chemistry. The driven turbulence simulations of Glover & Mac Low (2007b) identified moderate amounts of molecular hydrogen to be out of chemical equilibrium, a finding they attributed to turbulent transport of H_2 from high- to low-density gas that occurs on a shorter timescale than the chemistry can readjust. This same type of mass transport would likely occur within other large-scale simulations. Similarly, the colliding flow simulations of Valdivia et al. (2015) show the assumption of chemical equilibrium can under- or over-predict the true H_2 abundance depending on density range and integration time, with the largest discrepancies occurring at early times and, interestingly, high densities.

While the assumption of chemical equilibrium likely overestimates the H_2 fraction, particularly at low densities, the amount of CO is likely *underestimated* due to the supernovae feedback prescription in K15. As discussed in Section 3.1, supernovae events in K15 were modeled by injecting momentum the instant density exceeds the star formation threshold, rather than allowing any time delay. For the original purposes of K15, which focused on the properties of diffuse atomic gas that is the main ISM mass reservoir, the exact timing of supernovae events was unimportant compared to the ability for the supernovae rate to change in time in response to the ISM state. However, for the present purposes, this lack of a time delay tends to suppress the formation of large, dense structures where large CO abundances would be expected. Nonetheless, since our primary objective is to understand the role of radiative shielding and numerical approximations to it in determining the chemical balance of the ISM, and not to study the chemical balance itself, this limitation of the simulations does not significantly interfere with our goals.

In future work, we plan to utilize our best performing local model, one in which the temperature-capped Jeans length is used as a proxy for L_{shield} , to account for radiative shielding in time-dependent radiation-magneto-hydrodynamic AMR zoom-in simulations from galactic disk scales down to stellar cluster scales that will achieve significantly higher concentrations of dense, molecule rich gas than is present in the K15 snapshots. Post-processing these snapshots with the tools developed here will further validate the utility of such a local approximation to accurately model FUV radiative shielding and photo-regulated chemistry. We additionally plan to extend the radiative transfer post-processing analysis performed here to different physical systems, notably isolated, dwarf galaxies with sub-parsec resolution and densities approaching $10^4 - 10^5 \text{ cm}^{-3}$ (e.g., Goldbaum et al. 2015). In these targets of future analyses, the presence of more and much larger CO rich structures will permit the measurement of integrated line intensities, the X-factor, and their variation with metallicity and observation line-of-sight.

ACKNOWLEDGMENTS

This work was supported by NASA TCAN grant NNX-14AB52G (for CTSS, MRK, CK, ECO, JMS, SL, CFM, and RIK). RIK, MRK and CFM acknowledge support from NASA ATP grant NNX-13AB84G. CFM and RIK acknowledge support from NSF grant AST-1211729. RIK acknowledges support from the US Department of Energy at the Lawrence Livermore National Laboratory under contract DE-AC52-07NA27344.

REFERENCES

- Bakes E. L. O., Tielens A. G. G. M., 1994, *ApJ*, 427, 822
 Bergin E. A., Tafalla M., 2007, *ARA&A*, 45, 339
 Bialy S., Sternberg A., 2015, *MNRAS*, 450, 4424
 Bigiel F., Leroy A., Walter F., Brinks E., de Blok W. J. G., Madore B., Thornley M. D., 2008, *AJ*, 136, 2846
 Black J. H., van Dishoeck E. F., 1987, *ApJ*, 322, 412
 Bronfman L., Casassus S., May J., Nyman L.-Å., 2000, *AAP*, 358, 521
 Browning M. K., Tumlinson J., Shull J. M., 2003, *ApJ*, 582, 810
 Cen R., 1992, *ApJS*, 78, 341
 Chen C.-Y., Ostriker E. C., 2014, *ApJ*, 785, 69
 Chen C.-Y., Ostriker E. C., 2015, *ApJ*, 810, 126
 Clark P. C., Glover S. C. O., Klessen R. S., 2012, *MNRAS*, 420, 745
 Creasey P., Theuns T., Bower R. G., 2013, *MNRAS*, 429, 1922
 Davis S. W., Stone J. M., Jiang Y.-F., 2012, *ApJS*, 199, 9
 Dobbs C. L., Glover S. C. O., Clark P. C., Klessen R. S., 2008, *MNRAS*, 389, 1097
 Dobbs C. L. et al., 2014, *Protostars and Planets VI*, 3
 Draine B. T., 1978, *ApJS*, 36, 595
 Draine B. T., 2011, *Physics of the Interstellar and Intergalactic Medium*. Princeton University Press: Princeton, NJ
 Draine B. T., Bertoldi F., 1996, *ApJ*, 468, 269
 Fall S. M., Chandar R., 2012, *ApJ*, 752, 96
 Federman S. R., Glassgold A. E., Kwan J., 1979, *ApJ*, 227, 466
 Founesneau M. et al., 2014, *ApJ*, 786, 117
 Gent F. A., Shukurov A., Fletcher A., Sarson G. R., Mantere M. J., 2013, *MNRAS*, 432, 1396
 Glassgold A. E., Galli D., Padovani M., 2012, *ApJ*, 756, 157
 Glover S. C. O., Clark P. C., 2012a, *MNRAS*, 421, 9
 Glover S. C. O., Clark P. C., 2012b, *MNRAS*, 426, 377
 Glover S. C. O., Federrath C., Mac Low M.-M., Klessen R. S., 2010, *MNRAS*, 404, 2
 Glover S. C. O., Jappsen A.-K., 2007, *ApJ*, 666, 1
 Glover S. C. O., Mac Low M.-M., 2007a, *ApJS*, 169, 239
 Glover S. C. O., Mac Low M.-M., 2007b, *ApJ*, 659, 1317
 Gnedin N. Y., Tassis K., Kravtsov A. V., 2009, *ApJ*, 697, 55
 Goldbaum N. J., Krumholz M. R., Forbes J. C., 2015, *ArXiv e-prints*, 1510.08458
 Goldsmith P. F., 2001, *ApJ*, 557, 736
 Górski K. M., Hivon E., Banday A. J., Wandelt B. D., Hansen F. K., Reinecke M., Bartelmann M., 2005, *ApJ*, 622, 759
 Greif T. H., Springel V., Bromm V., 2013, *ArXiv e-prints*, 1305.0823
 Greif T. H., Springel V., White S. D. M., Glover S. C. O., Clark P. C., Smith R. J., Klessen R. S., Bromm V., 2011, *ApJ*, 737, 75
 Habing H. J., 1968, *Bull. Ast. Inst. Neth.*, 19, 421
 Hennebelle P., Iffrig O., 2014, *AAP*, 570, A81
 Hill A. S., Joung M. R., Mac Low M.-M., Benjamin R. A., Haffner L. M., Klingenberg C., Waagan K., 2012, *ApJ*, 750, 104
 Hollenbach D. J., Tielens A. G. G. M., 1999, *Reviews of Modern Physics*, 71, 173
 Hopkins P. F., Quataert E., Murray N., 2011, *MNRAS*, 417, 950
 Indriolo N., McCall B. J., 2012, *ApJ*, 745, 91
 Joung M. K. R., Mac Low M.-M., 2006, *ApJ*, 653, 1266
 Kennicutt, Jr. R. C. et al., 2007, *ApJ*, 671, 333
 Kim C.-G., Kim W.-T., Ostriker E. C., 2011, *ApJ*, 743, 25

- Kim C.-G., Ostriker E. C., 2015a, *ApJ*, 802, 99
Kim C.-G., Ostriker E. C., 2015b, *ApJ*, 815, 67
Kim C.-G., Ostriker E. C., Kim W.-T., 2013, *ApJ*, 776, 1
Koyama H., Inutsuka S.-I., 2000, *ApJ*, 532, 980
Krumholz M. R., 2012, *ApJ*, 759, 9
Krumholz M. R., 2014, *MNRAS*, 437, 1662
Krumholz M. R., Klein R. I., McKee C. F., Bolstad J., 2007, *ApJ*, 667, 626
Krumholz M. R., Leroy A. K., McKee C. F., 2011, *ApJ*, 731, 25
Krumholz M. R., McKee C. F., Tumlinson J., 2008, *ApJ*, 689, 865
Krumholz M. R., McKee C. F., Tumlinson J., 2009, *ApJ*, 693, 216
Lee H.-H., Herbst E., Pineau des Forets G., Roueff E., Le Bourlot J., 1996, *AAP*, 311, 690
Leroy A. K., Walter F., Brinks E., Bigiel F., de Blok W. J. G., Madore B., Thornley M. D., 2008, *AJ*, 136, 2782
Leroy A. K. et al., 2013, *AJ*, 146, 19
Li P. S., Myers A., McKee C. F., 2012, *ApJ*, 760, 33
Mac Low M.-M., Glover S. C. O., 2012, *ApJ*, 746, 135
McKee C. F., Krumholz M. R., 2010, *ApJ*, 709, 308
Neufeld D. A., Lepp S., Melnick G. J., 1995, *ApJS*, 100, 132
Ostriker E. C., McKee C. F., Leroy A. K., 2010, *ApJ*, 721, 975
Rijkhorst E.-J., Plewa T., Dubey A., Mellema G., 2006, *AAP*, 452, 907
Safrank-Shrader C., Montgomery M., Milosavljevic M., Bromm V., 2015, *ArXiv e-prints*, 1501.03212
Saintonge A. et al., 2011a, *MNRAS*, 415, 32
Saintonge A. et al., 2011b, *MNRAS*, 61
Shetty R., Ostriker E. C., 2012, *ApJ*, 754, 2
Smith R. J., Glover S. C. O., Clark P. C., Klessen R. S., Springel V., 2014, *MNRAS*, 441, 1628
Sobolev V. V., 1960, *Moving envelopes of stars*. Cambridge: Harvard University Press
Stacy A., Greif T. H., Klessen R. S., Bromm V., Loeb A., 2013, *MNRAS*, 431, 1470
Sternberg A., 1988, *ApJ*, 332, 400
Sternberg A., Le Petit F., Roueff E., Le Bourlot J., 2014, *ApJ*, 790, 10
Stone J. M., Gardiner T. A., Teuben P., Hawley J. F., Simon J. B., 2008, *ApJS*, 178, 137
Valdivia V., Hennebelle P., G erin M., Lesaffre P., 2015, *ArXiv e-prints*, 1512.05523
van Dishoeck E. F., Black J. H., 1986, *ApJS*, 62, 109
van Dishoeck E. F., Black J. H., 1988, *ApJ*, 334, 771
Walch S. K. et al., 2014, *ArXiv e-prints*, 1412.2749
Wise J. H., Abel T., 2011, *MNRAS*, 414, 3458
Wolfire M. G., Hollenbach D., McKee C. F., 2010, *ApJ*, 716, 1191
Wong T., Blitz L., 2002, *ApJ*, 569, 157
Yoshida N., Omukai K., Hernquist L., Abel T., 2006, *ApJ*, 652, 6